Monthly Notices
of the
ROYAL ASTRONOMICAL SOCIETY

Mon. Not. R. Astron. Soc. **418,** 2386–2402 (2011) doi:10.1111/j.1365-2966.2011.19634.x

Herschel⋆ observations of the Centaurus cluster – the dynamics of cold gas in a cool core

R. Mittal,[1]† C. P. O'Dea,[2] G. Ferland,[3] J. B. R. Oonk,[4,5] A. C. Edge,[6] R. E. A. Canning,[7] H. Russell,[8] S. A. Baum,[1] H. Böhringer,[9] F. Combes,[10] M. Donahue,[11] A. C. Fabian,[7] N. A. Hatch,[12] A. Hoffer,[11] R. Johnstone,[7] B. R. McNamara,[8,13,14] P. Salomé[10] and G. Tremblay[15]

[1]*Chester F. Carlson Center for Imaging Science, Rochester Institute of Technology, Rochester, NY 14623, USA*
[2]*Department of Physics, Rochester Institute of Technology, 84 Lomb Memorial Drive, Rochester, NY 14623, USA*
[3]*Department of Physics, University of Kentucky, Lexington, KY 40506, USA*
[4]*Leiden Observatory, Leiden University, P. B. 9513, Leiden 2300 RA, the Netherlands*
[5]*Netherlands Institute for Radio Astronomy, Postbus 2, 7990 AA Dwingeloo, the Netherlands*
[6]*Institute for Computational Cosmology, Department of Physics, Durham University, Durham DH1 3LE*
[7]*Institute of Astronomy, Madingley Road, Cambridge CB3 0HA*
[8]*Department of Physics & Astronomy, University of Waterloo, ON N2L 3G1, Canada*
[9]*Max-Planck-Institut für extraterrestrische Physik, 85748 Garching, Germany*
[10]*Observatoire de Paris, LERMA, CNRS, 61 Av. de l' Observatoire, 75014 Paris, France*
[11]*Physics and Astronomy Department, Michigan State University, East Lansing, MI 48824, USA*
[12]*School of Physics and Astronomy, University of Nottingham, University Park, Nottingham NG7 2RD*
[13]*Perimeter Institute for Theoretical Physics, Waterloo, Canada*
[14]*Harvard–Smithsonian Center for Astrophysics, 60 Garden Street, Cambridge, MA 02138, USA*
[15]*Astrophysical Science and Technology, Rochester Institute of Technology, Rochester, NY 14623, USA*

Accepted 2011 August 12. Received 2011 August 1; in original form 2011 May 20

ABSTRACT

Brightest cluster galaxies (BCGs) in the cores of galaxy clusters have distinctly different properties from other low-redshift massive ellipticals. The majority of the BCGs in cool-core clusters show signs of active star formation. We present observations of NGC 4696, the BCG of the Centaurus galaxy cluster, at far-infrared (FIR) wavelengths with the *Herschel* space telescope. Using the PACS spectrometer, we detect the two strongest coolants of the interstellar medium, [C II] at 157.74 μm and [O I] at 63.18 μm, and in addition [N II] at 121.90 μm. The [C II] emission is extended over a region of 7 kpc with a similar spatial morphology and kinematics to the optical Hα emission. This has the profound implication that the optical hydrogen recombination line, Hα, the optical forbidden lines, [N II] λ6583 Å, the soft X-ray filaments and the FIR [C II] line all have the same energy source.

We also detect dust emission using the PACS and SPIRE photometers at all six wavebands. We perform a detailed spectral energy distribution fitting using a two-component modified blackbody function and find a cold 19-K dust component with mass $1.6 \times 10^6\,M_\odot$ and a warm 46-K dust component with mass $4.0 \times 10^3\,M_\odot$. The total FIR luminosity between 8 and 1000 μm is $7.5 \times 10^8\,L_\odot$, which using Kennicutt relation yields a low star formation rate of $0.13\,M_\odot\,yr^{-1}$. This value is consistent with values derived from other tracers, such as ultraviolet emission. Combining the spectroscopic and photometric results together with optical Hα, we model emitting clouds consisting of photodissociation regions adjacent to ionized regions. We show that in addition to old and young stellar populations, there is another

⋆*Herschel* is an ESA space observatory with science instruments provided by European-led Principal Investigator consortia and with important participation from NASA.

†E-mail: rmittal@astro.rit.edu

source of energy, such as cosmic rays, shocks or reconnection diffusion, required to excite the Hα and [C II] filaments.

Key words: photodissociation region (PDR) – galaxies: active – galaxies: clusters: intracluster medium – galaxies: kinematics and dynamics – galaxies: star formation – infrared: ISM.

1 INTRODUCTION

Clusters of galaxies offer us a unique opportunity to study astrophysical components on widely differing scales. Intensive theoretical and observational efforts have revealed that these components are closely tied to one another. The megaparsec-scale intracluster medium (ICM) is a hot plasma emitting bremsstrahlung X-ray radiation. The central regions of this plasma ($\leq$300 kpc) have high electron densities; hence the numerous observed clusters with peaked surface brightness profiles. Such high gas densities imply rapid gas cooling ($\ll 1/H_0$) leading to a steady, mass deposition rate (tens to a few hundreds $M_\odot\ yr^{-1}$) (e.g. Fabian 1994) and iteratively increasing central densities.

However, this picture is far from complete. High-resolution *XMM–Newton* spectral and *Chandra* imaging of cool-core (CC) clusters (e.g. Kaastra et al. 2001; Peterson et al. 2001, 2003; Tamura et al. 2001; Sakelliou et al. 2002; Xu et al. 2002; Sanders et al. 2008; Hudson et al. 2010) have shown very little cool gas in their cores with the central temperatures no lower than a fifth of the virial temperature. Heating by clustercentric active galactic nuclei (AGN) through outflows (possibly in conjunction with other processes like heat conduction, cosmic ray heating and convection) appears to be an irreplaceable heating mechanism that prevents the gas from undergoing excessive cooling (e.g. Binney & Tabor 1995; Churazov et al. 2002; Roychowdhury et al. 2004; Voit & Donahue 2005). Several studies have established morphological, statistical and physical correlations between X-ray properties of CC clusters and AGN at their centres (Burns 1990; Bîrzan et al. 2004; Dunn & Fabian 2006; Peterson & Fabian 2006; Rafferty et al. 2006; Edwards et al. 2007; McNamara & Nulsen 2007; Mittal et al. 2009) that support AGN as the primary heating candidates.

Despite AGN and other plausible sources of heating which stop the ICM from cooling catastrophically, recent observations of many ($\sim$40) brightest cluster galaxies (BCGs) show that the ICM gas *is* cooling but at a much suppressed level. They appear to have substantial amount of cold gas, of which a small fraction is forming stars (e.g. Johnstone, Fabian & Nulsen 1987; McNamara et al. 1989; Allen 1995; Mittaz et al. 2001; Edge & Frayer 2003; O'Dea et al. 2004, 2008, 2010; Hicks & Mushotzky 2005). It seems that the cold gas is able to somehow survive for long periods of time.

A significant number of CC clusters show optical line filaments, such as in A 426 (Perseus, Conselice et al. 2001), A 1795 (Crawford, Sanders & Fabian 2005a). Crawford et al. (1999) did an optical study of >250 dominant galaxies in X-ray-selected galaxy clusters and showed that about 25 per cent of them have Hα emission line in their spectra with intensity ratios typical of cooling flow nebulae (also see Hu, Cowie & Wang 1985; Heckman et al. 1989). Amidst these exciting discoveries of Hα, Canning et al. (2011a) have detected the optical coronal line emission [Fe X] λ 6374 Å in NGC 4696 using VIsible MultiObject Spectrograph (VIMOS) spectra, implying yet another component of gas at temperatures in the range (1–5) $\times$ 10^6 K (also see Oegerle et al. 2001; Bregman et al. 2006). Warm molecular H_2 at $\sim$2000 K (Jaffe & Bremer 1997; Donahue et al. 2000; Edge et al. 2002; Hatch et al. 2005), cold molecular H_2 at 300–400 K (Johnstone et al. 2007) and cold CO gas at few tens of kelvin (Edge 2001; Salomé et al. 2008) also exist in the cores and in regions overlapping with the extended optical filaments. Edge (2001) detected 16 CC clusters with IRAM and JCMT, implying a substantial mass (10^9–$10^{11.5}$) $M_\odot$ of molecular gas within 50-kpc radius of the BCGs. Similarly, Salomé & Combes (2003) studied 32 BCGs in CC clusters with the IRAM 30-m telescope and found gas masses between 3×10^8 and 4×10^{10} $M_\odot$.

From the above observations of CC clusters, it is clear that there are different components of gas at almost every temperature in the range varying from the virial temperature of the ICM (10^7 K) to the temperature of the star-forming molecular clouds (10 K). An important result from the point of view of energetics of the observed warm molecular hydrogen emission and also the optical coronal emission line is that these emissions are very likely due to the gas being reheated rather than cooling out of the ICM (Donahue et al. 2000; Canning et al. 2011a). The molecular H_2 emission, for example, is too bright to arise from gas cooling out of the ICM. Based on the measured H_2 line luminosity and assuming the fraction of cooling in the line emission, η = 2–10 per cent, the estimated mass cooling rate is two orders of magnitude larger than the mass deposition rate predicted from the X-ray surface brightness profile. Understanding the details of how the mass and energy transfer occurs is crucial. To that end, a key component is the molecular gas and dust at <60 K, whose natural emission is accessible by *Herschel*.

In this paper, we study NGC 4696, the brightest galaxy of the Centaurus cluster of galaxies (Abell 3526). This work is a part of a *Herschel* Open Time Key Project devoted to study cold gas and dust in 11 BCGs. Preliminary results of this study can be found in Edge et al. (2010a,b). NGC 4696 is at a redshift of 0.010 16 (Postman & Lauer 1995) corresponding to a radial velocity of 3045 km s^{-1}. Owing to its proximity, this cluster has been a subject of numerous studies (e.g. Fabian et al. 1982; Lucey, Currie & Dickens 1986; Sparks, Macchetto & Golombek 1989; de Jong et al. 1990; Allen & Fabian 1994; O'Dea et al. 1994; Sparks, Carollo & Macchetto 1997; Laine et al. 2003; Crawford et al. 2005b; Taylor et al. 2006; Johnstone et al. 2007; Farage et al. 2010; Canning et al. 2011a). The *Chandra* X-ray observations show a bright dense core with plume-like structures that spiral off clockwise to the north-east. It is a classic CC cluster based on its short central [at 5 kpc ($0.004R_{500}$)][1] cooling time (<0.5 Gyr). However, the expected gas mass deposition rate within the cooling region is relatively small, $\sim$ a few tens of solar masses per year (Fabian et al. 1982; Ikebe et al. 1999; Sanders & Fabian 2002; Hudson et al. 2010). Detailed *XMM–Newton* Reflection Grating Spectrometer (RGS) observations indicate the presence of cool gas at the centre of the cluster with temperature in the range of 0.35–3.7 keV. Optical observations reveal bright line-emitting filaments in [N II] λ6583 Å and Hα, which were first discovered by Fabian et al. (1982) and have been mapped more recently using the EMMI instrument on the 3.58-m New Technology Telescope (NTT) with a much higher resolution by Crawford et al. (2005b). These filaments extend out in a similar manner to the spiral structure seen

[1] R_{500} is the radius within which the average mass density of the cluster is 500 times the critical density of the Universe.

in the X-ray. They also show a remarkable spatial correlation with the dust features, in particular the dust lane seen looping around the core of NGC 4696 (Sparks et al. 1989; Laine et al. 2003).

NGC 4696 is a host to the low-power steep-spectrum Fanaroff–Riley type I radio source, PKS 1246−410 (e.g. Taylor et al. 2006). The total radio luminosity of the radio source is 9.43×10^{40} erg s^{-1} (Mittal et al. 2009). The radio core coincides well with the duo-core optical nucleus revealed by the high-resolution *Hubble Space Telescope* (*HST*) imaging. The radio emission shows a one-sided jet oriented to the south on small (30 pc) scales that evolves into lobes oriented east–west on kpc scales (Taylor et al. 2006). The total extent of the lobes along the east–west direction is about 10 kpc, after which both the lobes eventually turn south. The radio plasma is clearly interacting with the hot X-ray gas and seems to be correlated with the X-ray cavities.

We describe the *Herschel* observations and data reduction in Section 2 and the results in Section 3. We present an analysis of the AGN contribution and kinematics in Section 4 and a detailed modelling of the photodissociation region (PDR) in Section 5. We give our final conclusions in Section 6 and a summary of this study in Section 7. We assume throughout this paper the Λ cold dark matter concordance Universe, with $H_0 = 71\,h_{71}$ km s^{-1} Mpc^{-1}, $\Omega_{\rm m} = 0.27$ and $\Omega_\Lambda = 0.73$. This translates into a physical scale of 1 arcsec = 0.2 kpc at the redshift of NGC 4696.

2 *Herschel* OBSERVATIONS AND DATA ANALYSIS

We used the ESA *Herschel Space Observatory* (Pilbratt et al. 2010) using the Photodetector Array Camera and Spectrometer (PACS; Poglitsch et al. 2010) and the Spectral and Photometric Imaging Receiver (SPIRE; Griffin et al. 2010) to study the cold phase (<60 K) of the interstellar medium (ISM) and ICM. The aim of these observations was to understand the details of mass and energy transfer between the different phases of gas. In particular, we study PDRs which are relatively small in volume-filling factor but owing to high densities (and thermal pressures) as compared to that of the average ISM dominate the radiation of a galaxy (e.g. Hollenbach & Tielens 1999). PDRs define the emission characteristics of the ISM and star formation regions in a galaxy. They primarily comprise molecular hydrogen, ionized carbon, neutral oxygen, CO and dust, such as silicates, silicate carbides, polycyclic aromatic hydrocarbons (PAHs), etc. Detailed PDR descriptions and chemical processes can be found in, e.g., Hollenbach & Tielens (1999), Kaufman et al. (1999) and Röllig et al. (2007).

2.1 PACS spectrometry

We observed the two primary coolants of the neutral ISM, the [C II] line at 157.74 μm and the [O I] line at 63.18 μm, along with [O IB] at 145.52 μm, [Si I] at 68.470 μm, [N II] at 121.90 μm and [O III] at 88.36 μm with the PACS spectrometer on *Herschel*. The $^2P_{3/2} \rightarrow {}^2P_{1/2}$ fine-structure emission line of [C II] is very often the brightest emission line in galaxy spectra, followed by the [N II] lines at 122 μm ($^3P_2 \rightarrow {}^3P_1$) and 205 μm ($^3P_1 \rightarrow {}^3P_0$). Ionized nitrogen and oxygen are mainly produced in warm ionized medium, such as H II regions, and so the [N II] 122-μm and the [O III] 88.36-μm lines can be used to obtain constraints on the fractions of ionized and neutral media.

All lines were observed in the line spectroscopy mode with the chopping and nodding implementation to subtract the rapidly varying telescope background and dark current. The details of the observational parameters are summarized in Table 1. We used the large chopper throw throughout, such that the mirror chops two regions of sky 6 arcsec apart alternately. While [O I] and [C II] observations were made in the raster-mapping mode, all the other line observations were made in the pointed mode with a field of view of 47 × 47 arcsec^2. The PACS spectrometer contains an image slicer unit for integral field spectroscopy. The slicer transforms a 5 × 5 pixel focal plane image into a linear array of 25 spatial pixels termed *spaxels*, each 9.4 × 9.4 arcsec^2 in size. This technique ensures high sensitivity to detecting weak emission lines and provides simultaneous spectra of all extended emission in the field of view. The signal from each spaxel then goes through the grating assembly resulting in 16 spectral elements. The PACS spectrometer has two channels, red (51–105) μm and blue (102–220) μm, which can be operated at the same time. This allowed us to perform sequential observations of both [O I] and [C II]. The raster mapping consisted of a 3 × 3 array of overlapping single pointings (three raster lines and three points per line) separated by 23.5 arcsec in both the directions, along and orthogonal to the raster lines.

We applied the standard pipeline routines described in the PACS data-reduction guideline (PDRG) to process the data from their raw state (level 0) to a fully calibrated state (level 2), using the Herschel Interactive Processing Environment (HIPE; Ott 2010) version 3.0 CIB 1475. The data-reduction steps included removing cosmic ray glitches and correcting for the intrinsic non-linearities. We used the ground-based flat-field estimates to correct for the pixel responses, which are known to overestimate the fluxes. We followed the PACS spectroscopy performance and calibration (PSPC) memo to correct the fluxes by applying factors of 1.3 for the blue band and 1.1 for the red band. The penultimate final PACS data product is in the form of two 5 × 5 × *n* cubes, corresponding to the two nodding positions, where *n* is the number of wavelengths present. This product is further rebinned in wavelength in accordance with the actual wavelengths present and the user-requested resolution (see Section 2.1.1). The PACS spatial resolution varies from 11.3 arcsec for the [C II] 157.74-μm line to 4.5 arcsec for the [O I] 63.18-μm line.

Table 1. *Herschel* PACS spectroscopy observational log of NGC 4696 at a redshift of 0.010 16. All the lines were observed in the line spectroscopy mode and on the same day: 2009 December 30.

Line	Peak rest λ (μm)	ObsID	Duration (s)	Bandwidth (μm)	Bandwidth (km s^{-1})	Spectral (μm)	FWHM (km s^{-1})	Spatial FWHM (arcsec)	Mode
O I	63.180	1342188700	6912	0.266	1250	0.017	79	4.6	3 × 3 raster, step size 23.5 arcsec
C II	157.74	1342188700	3096	1.499	2820	0.126	237	11.5	3 × 3 raster, step size 23.5 arcsec
N II	121.90	1342188701	3440	1.717	4180	0.116	280	8.9	Pointed
O III	88.36	1342188701	3680	0.495	1660	0.033	110	6.4	Pointed
O IB	145.52	1342188702	3440	1.576	3215	0.123	250	10.5	Pointed
Si I	68.47	1342188702	3840	0.218	945	0.014	62	4.9	Pointed

2.1.1 Oversampling and upsampling factors

As mentioned above, the $5 \times 5 \times n$ cubes are further rebinned in wavelength by applying two factors called 'oversample' and 'upsample'. The oversample factor increases the number of bins over which the data are averaged to create a spectrum, and the upsample factor specifies the shift in wavelength in the units of the bin width. The default values, oversample = 2 and upsample = 1, correspond to the signal sampled at the Nyquist–Shannon rate, yielding the instrument spectral resolution at that wavelength. Increasing the upsample factor, for example, to upsample = 2 yields two spectra, both adhering to the instrument resolution but shifted by half a bin width with respect to each other. An upsample factor greater than unity may be used to identify features narrower than the instrument resolution in the line profile but at the expense of increased noise. Lastly, the combination of oversample = 1 and upsample = 1 undersamples the data to render a spectral resolution a factor of 2 coarser than the original one, hence affecting the full width at half-maximum (FWHM) of the fitted line. We investigated various combinations of oversample and upsample factors for each of the lines to optimize the signal-to-noise ratio (S/N) and the spectral resolution.

2.1.2 Line flux estimation

In the case of emission well centred on the central spaxel, a wavelength-dependent point source correction factor has to be applied to the measured line flux density to account for the fraction of the beam that is lost to the neighbouring spaxels (beam spillover). An alternate way of recovering the flux in the entire beam is to co-add the spectra obtained in different spaxels, but this method suffers from the risk of line distortion. A yet alternate method is to keep the spectra separate and add only the fluxes contained in the spaxels with significant point source contribution. This method works well also for slightly extended sources provided that the emission is fully contained within the central few spaxels of the pointing. However, in case of extended emission spread over more than a single pointing (47×47 arcsec^2), we used the HIPE inbuilt task 'specProject' for obtaining the integrated line flux. This algorithm involves a projection of all the positions in the input cube on to the sky. It calculates a regular right ascension (RA)/declination (Dec.) grid with a default spaxel size of 3 arcsec and projects the raster positions on to it. The details of this algorithm can be found in the spectroscopy pipeline described in the PDRG documentation. Thereafter, we conducted 'aperture photometry' by placing a rectangular box around the visible emission and by integrating the flux to obtain a spectrum. Since none of our observations was performed in dithered mode, the main necessity of using 'specProject' was to obtain a projection of the multiple single pointings on the sky plane. Since the individual pointings overlap by a considerable amount, simply adding the fluxes in all spaxels contributing above a certain threshold results in an overestimation of the line emission.

We used the Levenberg–Marquardt minimization routine (Levenberg 1944; Marquardt 1963) to fit a model to an observed spectrum. The model comprised a Gaussian for the line emission and a polynomial of order 0 (or 1) for the pseudo-continuum[2] baseline. A positive line detection was based in terms of the S/N. The S/N was defined as the ratio of the line peak to the standard deviation of the data about the fitted model.

[2] Presently, there are offsets in the continuum levels between the different spaxels preventing the extraction of reliable continuum data.

2.2 PACS photometry

The PACS photometric observations were taken in large scan mapping mode in all three bands of the photometer, blue-short (BS) (70 μm), blue-long (BL) (100 μm) and red (R) (160 μm) using the medium scan speed (20 arcsec s^{-1}). The scan maps comprised 18 scan line legs of 4-arcmin length and cross-scan step of 15 arcsec. Each observation had a 'scan' and an orthogonal 'cross-scan' direction, and we calibrated the corresponding data separately before combining them into a single map of 9×9 arcmin^2. The resulting maps have a resolution of 5.2, 7.7 and 12 arcsec at 70, 100 and 160 μm. The PACS photometer performs dual-band imaging such that the BS and BL bands each has simultaneous observations in the R band, so we have two sets of scans in the R band.

For PACS photometry, we used the HIPE version 3.0 CIB 1475 to reduce the data and adopted the PDRG to process the raw level-0 data to calibrated level 2 products. We employed the official script for PACS ScanMapping mode with particular attention to the high pass filtering to remove '$1/\sqrt{f}$' noise. We used the 'HighPassFilter' method to remove the large-scale ($\gtrsim$80 arcsec) artefacts. The target BCG and other bright sources in the field were masked prior to applying the filter. The size of the mask was chosen to be less than the filter size so as to minimize any leftover low-frequency artefacts under the masks. We used a filter size of 20 readouts for the BS and BL bands and 30 readouts for the R band and a mask radius of 20 arcsec for the BS and BL bands and 30 arcsec for the R band. Finally, the task 'photProject' was used to project the calibrated data on to a map on the sky in units of Jy pixel^{-1}. The 'scan' and 'cross-scan' maps were then averaged together to produce the final co-added map.

2.3 SPIRE photometry

The SPIRE photometry was performed in the large scan map mode with cross-linked scans in two orthogonal scan directions. The photometer has a field of view of 4×8 arcmin^2, which is observed simultaneously in three spectral bands centered at approximately 250, 350 and 500μm, with a resolution of about 18, 25 and 36 arcsec, respectively.

For SPIRE photometry, we used a newer HIPE version 4.0 CIB 1432 and the standard HIPE pipeline for the LargeScanMap observing mode and the naïve map maker. The pre-processed raw telemetry data were first subject to engineering conversion wherein the raw timeline data were converted to meaningful units, the SPIRE pointing product was created, deglitching and temperature drift correction were performed and maps were created, the units of which were Jy beam^{-1}.

3 RESULTS

3.1 Line detections

Of the lines observed, we detected [O I], [C II] and [N II] in NGC 4696 (Fig. 1). We did not detect [Si I], [O III] and [O IB] emission lines at a 3σ level of 3.0×10^{-18} W m^{-2} for [Si I] and [O III], and 1.2×10^{-18} W m^{-2} for [O IB]. The line parameters are summarized in Table 2.

The [N II] emission line at 121.9 μm has been detected only in the central 9.4-arcsec spaxel. The [O I] emission-line spectrum at 63.18 μm, although noisy, has clearly been detected. Shown in the top left-hand panel of Fig. 1 is the continuum-subtracted spectrum integrated over a central region of ∼15 arcsec in diameter (3 kpc). Hence, the [O I] emission is slightly extended. The spectrum is

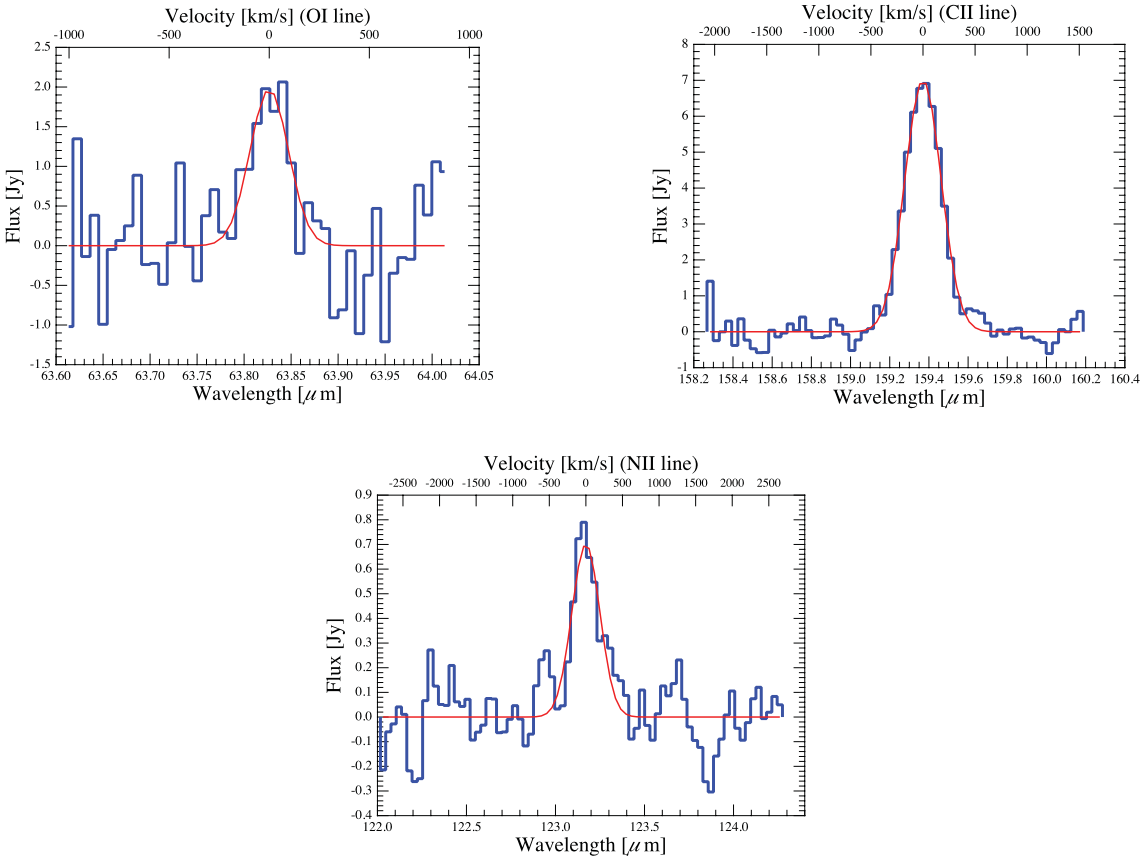

Figure 1. The forbidden FIR line detections in the centre of NGC 4696 made with the *Herschel* PACS instrument. The lines are spatially integrated: the [O I] 63.18-μm line (upper left-hand panel, marginally extended), the [C II] 157.74-μm line (upper right-hand panel, extended) and the [N II] 121.9-μm (lower panel, point-like).

Table 2. Estimated parameters for the FIR forbidden lines in NGC 4696. Also given are the upper limits on the line flux for the non-detections. The total extent of the [C II] and [O I] emission was estimated based on visual inspection.

Line	λ (μm)	Offset (km s^{-1})		FWHM (km s^{-1})		Line flux	Total extent
		z_{bcg}	z_{cl}	Obs.	Intrinsic	(10^{-18} W m^{-2})	(arcsec)
[O I]	63.827 ± 0.005	−15 ± 28	−52 ± 28	228 ± 54	218 ± 35	57.6 ± 7.7	15
[C II]	159.370 ± 0.003	18 ± 11	−22 ± 11	410 ± 13	335 ± 16	174.7 ± 3.1	35
[N II]	123.171 ± 0.009	48 ± 40	8 ± 40	452 ± 54	351 ± 69	24.9 ± 1.7	<9.4
[O III]	–	–	–	–	–	<3	–
[O IB]	–	–	–	–	–	<2	–
[Si I]	–	–	–	–	–	<4	–

obtained with oversample = 2 and upsample = 1 followed by the projection technique, 'specProject', described in Section 2.1.2.

The [C II] continuum-subtracted integrated line emission at 157.74 μm is shown in the top right-hand panel of Fig. 1. It is obtained using oversample = 1 and upsample = 4 and projecting the two nods on to the sky. Though oversample = 1 results in poorer instrumental resolution, it helps in beating down the noise and upsample = 2 or 4 helps recover some of the lost information. The two-dimensional distribution of [C II] emission is shown in the multiwavelength collage in Fig. 2, which contains an optical Hα image from NTT, an X-ray image from *Chandra* and 1.4-GHz radio contours from Very Large Array (VLA)/National Radio Astronomy Observatories (NRAO).[3] The *Chandra* data sets used to create the upper left-hand panel of Fig. 1 were ObsIds 504, 4954, 4955 and 5310, which were first presented in Sanders & Fabian (2002) and Fabian et al. (2002, 2005). The archival data sets were reprocessed with CIAO 4.3 and CALDB 4.4.0 to apply the appropriate gain and charge transfer inefficiency correction, then filtered to remove photons detected with bad grades and cleaned of flare periods. The final cleaned exposure time was 201.6 ks. Each of the final cleaned events files was then reprojected to match the position of the 4954 observation. A combined image was produced by summing images in the (0.5–1.0) keV band extracted from the individual reprojected data sets. This image was then corrected for exposure variation by dividing the summed image by summed exposure maps created for each data set.

The total extent of the [C II] emission is about 35 arcsec (7 kpc) in diameter. The [C II] image exhibits a north-west–south-east (NW–SE) elongation, which, in conjunction with the optical and

[3] The NRAO is a facility of the National Science Foundation operated under cooperative agreement by Associated Universities, Inc.

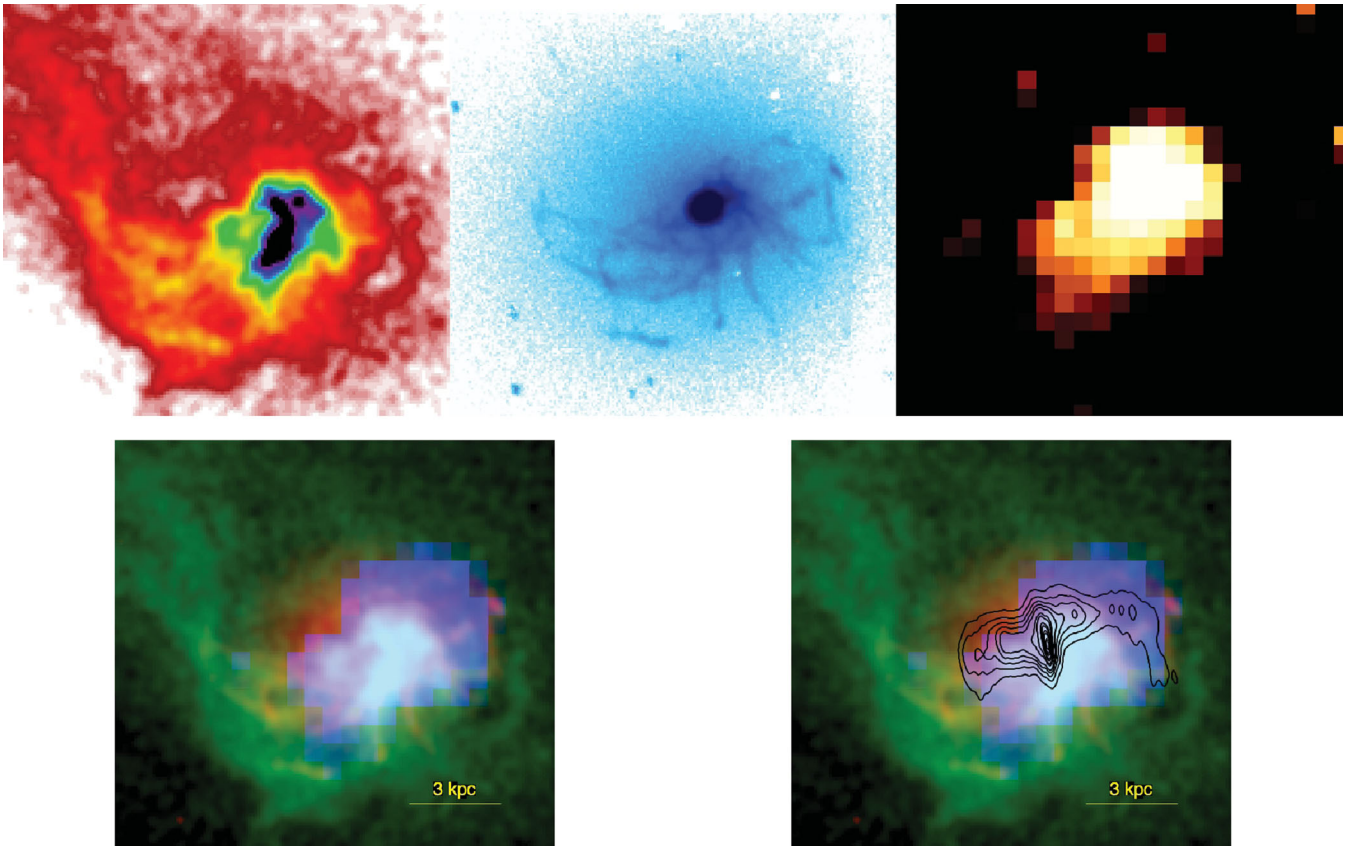

Figure 2. Upper panel: the *Chandra* X-ray surface brightness map in the soft energy band (0.5–1) keV (left), the Gemini optical Hα emission (middle; Crawford et al. 2005b) and the *Herschel* FIR [C II] 157.74-μm emission (right). Lower panel: a multiwavelength image of NGC 4696 with contours. Red: optical Hα line emission. Green: X-ray emission. Blue: FIR [C II] emission. Black contours: VLA 1.4-GHz radio contours (NRAO/VLA image archive). Each side measures an arcminute corresponding to a linear scale of 12 kpc.

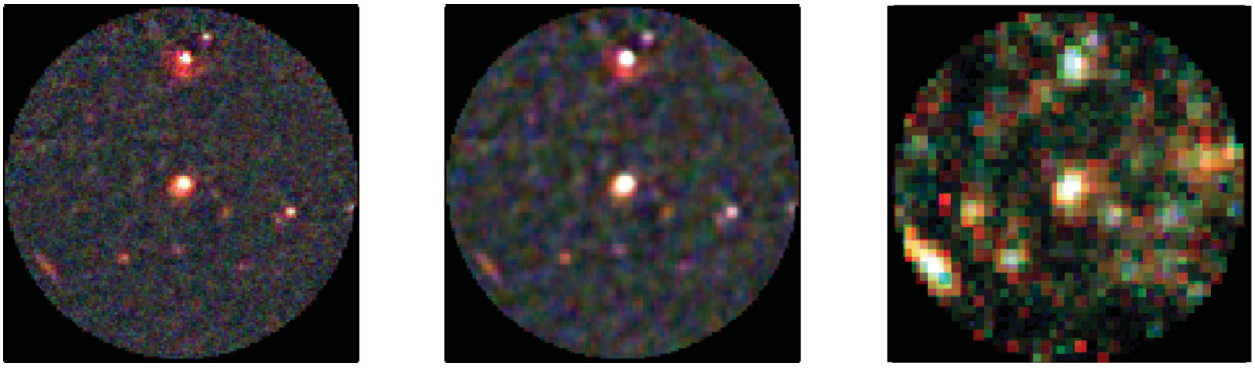

Figure 3. Photometry images of NGC 4696. Left: PACS colour images at 70 μm (blue), 100 μm (green) and 160 μm (red) with a resolution of 6, 7 and 12 arcsec, respectively. Centre: PACS colour images combined with the same smoothing Gaussian of FWHM 12 arcsec. Right: SPIRE colour images at 250 μm (blue), 350 μm (green) and 500 μm (red) with a resolution of 18, 24 and 38 arcsec, respectively. The image units are Jy beam^{-1} and each side measures 7 arcsec.

X-ray emission maps of the spiral filaments, is clearly the overall elongation direction associated with NGC 4696. The PACS continuum dust emission shows similar asymmetry about the centre of the galaxy (Fig. 3). The bulk of the [C II] emission appears to be displaced to the west relative to the Hα core. The centroid of the [C II] emission is indeed offset to the west of the Hα core by about 5 arcsec (half-spaxel size). The reported 1σ absolute pointing accuracy of *Herschel* is 2 arcsec for pointed observations and larger for scan map observations. As a check, we analysed the [C II] line observations with the latest official version of HIPE (6.0.2055) with updated calibration files and found a similar distribution of the [C II] emission with a similar offset from the Hα core. While the offset between the [C II] and Hα emission may also be real and reflect inhomogeneities in the ISM properties or different excitation mechanisms, given the similarity between [C II] and Hα it is more likely that the offset is due to the pointing uncertainty.

3.2 Aperture photometry

We conducted aperture photometry using a variety of different methods with the aim of attaining robust flux measurements and reliable uncertainties. These methods included routines inbuilt within HIPE, Graphical Astronomy and Image Analysis Tool (GAIA), etc. The

Table 3. Compilation of IR flux densities.

λ (μm)	Instrument	Aperture (arcsec)	Flux (mJy)
3.6	IRAC *Spitzer*[a]	65	328 ± 17
4.5	IRAC *Spitzer*[a]	65	191 ± 10
5.8	IRAC *Spitzer*[a]	65	162 ± 8
8.0	IRAC *Spitzer*[a]	65	100 ± 5
12	*IRAS*[b]		<25
24	MIPS *Spitzer*[a]	65	25.6 ± 3.0
24	MIPS *Spitzer*[c]	30	24 ± 4
25	*IRAS*[b]		<28
60	*IRAS*[b]		100 ± 23
70	MIPS *Spitzer*[a]	35	165 ± 33
70	MIPS *Spitzer*[c]	30	156 ± 19
70	PACS *Herschel*[d]	36	114 ± 11
100	PACS *Herschel*[d]	36	244 ± 24
100	*IRAS*[b]		830 ± 148
160	PACS *Herschel*[d]	36	383 ± 77
160	MIPS *Spitzer*[a]	40	256 ± 51
160	MIPS *Spitzer*[c]	30	331 ± 29
250	SPIRE *Herschel*[d]	38	208 ± 30
350	SPIRE *Herschel*[d]	38	98 ± 15
500	SPIRE *Herschel*[d]	38	38 ± 6

[a]The *Spitzer* IRAC/MIPS data are from a subsample of the ACCEPT sample of galaxy clusters (Hoffer et al., in preparation). The error bars reflect the absolute flux uncertainties.
[b]The *IRAS* data are from NASA/IPAC Extragalactic Data base (http://nedwww.ipac.caltech.edu).
[c]Kaneda, Onaka & Sakon (2005) and Kaneda et al. (2007).
[d]*Herschel* PACS/SPIRE data are from this work. The *Herschel* PACS/SPIRE error bars reflect the absolute flux uncertainties: 10 per cent at PACS BS and BL, and 20 per cent at R and 15 per cent at all SPIRE wavelengths.

spread in the flux estimates was within the random noise associated with the measurements.

For PACS flux densities, small aperture corrections were applied as outlined in the PACS ScanMap release note. Further flux calibration on the derived flux densities was performed to account for the known overestimation introduced by the ground-based flux calibration by factors of 1.05, 1.09 and 1.29 in the BS, BL and R bands, respectively. The PACS absolute flux accuracy is within 10 per cent for BS and BL, and better than 20 per cent for R. The uncertainties are not believed to be correlated due to the BS and BL bands being taken at different times and the R band using a different detector. Since we used a newer HIPE version to obtain SPIRE images, the known flux calibration offset was accounted for during the data conditioning and hence no multiplicative calibration factors were required. The SPIRE absolute flux accuracy is within 15 per cent for all the three bands. The flux measurements from *Herschel* and other instruments are given in Table 3.

Our *Herschel* flux estimate disagrees with the *Spitzer* MIPS 160-μm measurement of Hoffer et al. (in preparation), though it is consistent with the measurement of Kaneda et al. (2005). A systematic error in the performance of either of the two instruments can be ruled out since while at 70 μm the *Spitzer* flux estimate is higher than the *Herschel* estimate, at 160 μm the situation is reversed. In addition, we also ruled out the discrepancy being due to the difference in the spectral response functions of *Herschel* PACS and *Spitzer* MIPS photometers. We used the above-fitted spectral energy distribution (SED) of NGC 4696 as the 'true' source model and calculated the predicted flux density for each instrument as the weighted average, where the weights were determined from the spectral response function of each instrument. The *Herschel* PACS and *Spitzer* MIPS predicted flux densities at 70 and 160 μm estimated this way are consistent with each other to better than 5 per cent. Since the *Spitzer* MIPS 160-μm flux shows a spread between the measurements from Kaneda et al. (2005) and Hoffer et al. (in preparation), we give preference to the *Herschel* estimates, especially since *Herschel* is designed to operate at higher sensitivity at far-infrared (FIR) wavelengths.

3.3 Dust SED

The dust emission from NGC 4696 has been detected in all six PACS and SPIRE bands. In Fig. 3, we show the PACS images at 70, 100 and 160 μm, and the SPIRE images at 250, 350 and 500 μm centred on NGC 4696. The PACS photometry data-reduction pipeline described in Section 2.2 produces images with units Jy pixel^{-1}. We converted the units from Jy pixel^{-1} to Jy beam^{-1} by using the conversion factor $\pi/(4\ln 2)(\theta_{\rm beam}/\theta_{\rm pixel})^2$ pixel beam^{-1}, where $\theta_{\rm beam}$ is 6, 7 and 12 arcsec, and $\theta_{\rm pixel}$ is 3.2, 3.2 and 6.4 arcsec for the 70-, 100- and 160-μm bands, respectively.

The BCG emission seems to be slightly extended along the NW–SE direction. The origin of the IR continuum emission is the interstellar dust grains in the host galaxy, which are heated by the absorption of photons from an ionizing source. Whether this ionizing source is starbursts (SBs) or an AGN embedded in the host galaxy is usually a matter of debate, but the AGN/SB diagnostics for NGC 4696 suggest the AGN contribution to be very low (Section 4.1). We fitted the dust SED with a blackbody spectrum modified by a frequency-dependent emissivity. Following Aravena et al. (2008), and references therein, the flux density at a given frequency, ν, is

$$S_\nu = \frac{\Omega}{(1+z)^3}\,[B_\nu(T_{\rm d}) - B_\nu(T_{\rm cmb})]\,(1-{\rm e}^{-\tau_\nu(M_{\rm d})}), \quad (1)$$

where $B_\nu(T)$ is the Planck function at frequency ν and temperature T. $B_\nu(T_{\rm cmb})$ is the contribution from the cosmic microwave background at $T_{\rm cmb} = 2.73(1+z)$ K. Ω is the solid angle subtended by the source, $\pi\theta^2$, where θ is the source size in radians (here assumed to be the resolution of the PACS photometer at 70 μm). The last term in parenthesis is the modification to the blackbody radiation spectrum, where τ_ν is the dust optical depth,

$$\tau_\nu = \kappa_\nu \frac{M_{\rm d}}{D_{\rm A}^2\,\Omega}. \quad (2)$$

Here, $\kappa_\nu = 5.6 \times (\nu/3000\,{\rm GHz})^\beta$ m^2 kg^{-1} (Dunne et al. 2000) is the dust absorption coefficient and β is the dust emissivity index which we fixed to 2.

Motivated by the findings of Dunne & Eales (2001), we fitted the IR data with two modified blackbody functions, representing a cold dust component and a warm dust component. This gives four model parameters: the temperature and mass of the cold dust component, $T_{\rm d,c}$, $M_{\rm d,c}$, and the temperature and mass of the warm dust component, $T_{\rm d,w}$, $M_{\rm d,w}$. We used the Levenberg–Marquardt minimization routine from Numerical Recipes to obtain the best-fitting model parameters. We conducted the fit using seven data points: the six PACS and SPIRE photometer data and the *Spitzer* MIPS data at 24 μm. The *Spitzer* MIPS flux density at 24 μm receives a contribution from the hot dust component as well as the passive stellar population. In order to use the 24-μm data for the SED fitting, it is necessary to subtract the contribution from the passive stellar population. For this, we fitted a power law to the IRAC data, since the IRAC wavelengths are sensitive to emission from the old stellar population (OSP), and extrapolated the fit to 24 μm. The net flux

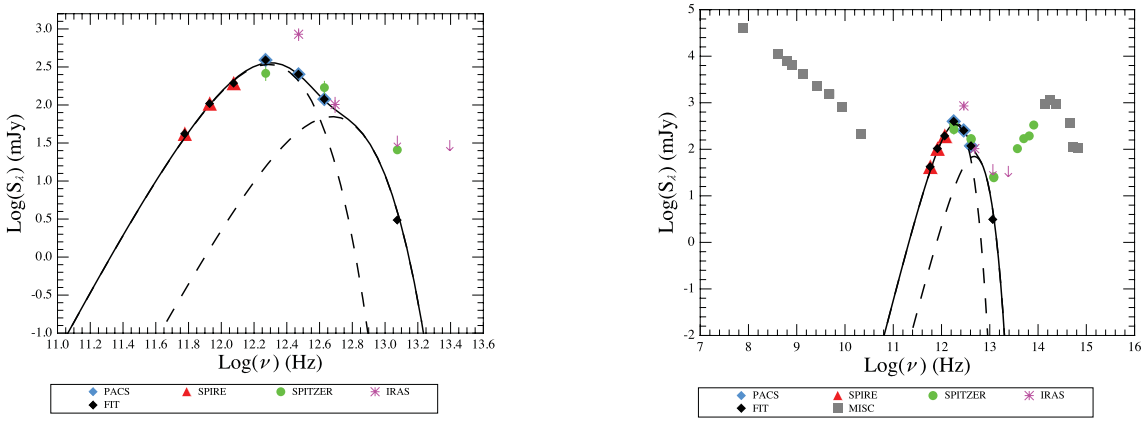

Figure 4. The SED of NGC 4696. Left: the FIR SED obtained from a modified two-component blackbody fit to the *Herschel* and *Spitzer* data, designated as 'FIT' (filled black diamonds). Right: the complete SED extending to radio frequencies on one end and optical and X-ray frequencies on the other, collectively designated as 'MISC'.

density after subtracting the contribution from the passive stellar population is 3.6 ± 3.0 mJy, which is significantly lower than the total observed value. It is this net flux density that we assigned to the hot dust component for the SED fitting.

The SED fitting yields a massive cold dust component with $T_{\rm d,c} = (18.9 \pm 0.7)$ K and $M_{\rm d,c} = (1.6 \pm 0.3) \times 10^6\,{\rm M}_\odot$ and a low-mass warmer dust component with $T_{\rm d,w} = (46.0 \pm 5.0)$ K and $M_{\rm d,w} = (4.0 \pm 2.8) \times 10^3\,{\rm M}_\odot$. As also seen in other studies, the cold component dominates the mass budget. The FIR and the total SEDs, the latter extending from radio to X-ray frequencies, are shown in Fig. 4. We used the fit parameters to estimate the total FIR luminosity of the dust between 8 and 1000 μm, $L_{\rm FIR,tot}$, and found it to be $(7.5 \pm 1.6) \times 10^8\,{\rm L}_\odot$. For the analysis of the PDRs described in Section 5, we used the FIR luminosity in the range 40–500 μm, which from here on is denoted by $L_{\rm FIR}$ and is equal to $(6.2 \pm 0.8) \times 10^8\,{\rm L}_\odot$.

To assess the robustness of the derived parameters and the quantities derived from them, such as the FIR luminosity, we also fitted the above model using the average of the two MIPS and one PACS flux estimates at each 70 and 160 μm. The fit results lead to a cold dust component with $T_{\rm d,c} = (18.2 \pm 0.8)$ K and $M_{\rm d,c} = (1.8 \pm 0.3) \times 10^6\,{\rm M}_\odot$, and a warm dust component with $T_{\rm d,w} = (43.0 \pm 4.7)$ K and $M_{\rm d,w} = (9.1 \pm 6.8) \times 10^3\,{\rm M}_\odot$. The inferred FIR luminosities are $L_{\rm FIR,tot} = (7.9 \pm 2.5) \times 10^8\,{\rm L}_\odot$ and $L_{\rm FIR} = (6.6 \pm 1.1) \times 10^8\,{\rm L}_\odot$. Hence, a variation of ∼20 per cent in the PACS flux densities results in about a 5–10 per cent variation in the total cold dust mass and the FIR luminosities. This is well within the formal error bars obtained from either of the two fitting methods.

3.4 Gas-to-dust mass ratio

O'Dea et al. (1994) searched for CO in a sample of five radio galaxies, including NGC 4696, using the Swedish-ESO Submillimeter Telescope. They reported non-detection in NGC 4696 and used the result to put limits on the gas mass. From these observations, the 3σ upper limit on the mass in the molecular gas is estimated to be $\sim 5 \times 10^8\,{\rm M}_\odot$. Using the dust mass calculated in Section 3.3, the (molecular) gas-to-dust mass ratio has an upper limit of ∼325. Note that the upper limit on the *total* gas-to-dust mass ratio is likely larger since the total-to-molecular gas mass ratio is greater than unity and may be as high as 5 (or more) depending upon parameters such as the ionization radiation intensity and the total hydrogen column density.

We also used the formalism laid out by Wolfire, Tielens & Hollenbach (1990), which uses the observed [C II] emission to obtain the atomic gas mass, assuming that the [C II] emission is optically thin:

$$M_{\rm g} = 2.7 \times 10^6 \left(\frac{D_{\rm L}}{1\ {\rm Mpc}}\right)^2 \left(\frac{F_{\rm C\,II}}{10^{-17}\ {\rm W\ cm^{-2}}}\right) \times \left(\frac{10^{-21}\ {\rm erg\ s^{-1}\ sr^{-1}\ atom^{-1}}}{\Lambda({\rm C\,II})}\right) \times \left(\frac{3 \times 10^{-4}}{x({\rm C\,II})}\right) {\rm M}_\odot, \quad (3)$$

where $D_{\rm L}$ is the luminosity distance, $F_{\rm C\,II}$ is the [C II] line flux, Λ(C II) is the cooling rate of ionized carbon and x(C II) is the abundance of ionized carbon relative to hydrogen. Most of the [C II] emission originates from the surface layers of the PDRs with the visual extinction, $A_{\rm V} < 4$, depleting steadily with increasing $A_{\rm V}$, and is the dominant of the three most important carbon-bearing species, C, C II and CO (Hollenbach, Takahashi & Tielens 1991). Hence the C II abundance can be equated to the elemental abundance of carbon, which, for the simulations of the PDRs described in Section 5, equals 2.5 times the interstellar value, $x({\rm C\,II}) = 6.3 \times 10^{-4}$. For gas temperatures higher than 100 K (the excitation temperature of C II is 92 K) and gas densities between 100 and 1000 cm^{-3}, Λ(C II) is in the range $(10^{-21}$ to $10^{-22})$ erg s^{-1} sr^{-1} atom^{-1}. Substituting these values into equation (3) gives a gas mass in the range (0.5–5) $\times 10^7\,{\rm M}_\odot$. This is consistent with the upper limit derived from the non-detection of CO by O'Dea et al. (1994).

The gas-to-dust mass ratio based on the above estimate of the gas mass is between 1 and 70. In comparison with the gas-to-dust mass ratios derived for other BCGs (Edge 2001; Edge et al. 2010a), which have typical values of a few hundred, the ratio in NGC 4696 is significantly lower. Note that the above method of determining the gas mass is not very robust for low n and $G0$, which is the case of NGC 4696 (see Section 5), and the dust mass is very sensitive to the assumed dust temperature, so the derived range of the gas-to-dust mass ratio should only be treated as a crude estimate.

3.5 Star formation rates

Assuming the dust heating to be due to the young stellar population (YSP) and high dust opacity in the star-forming regions, the Kennicutt relation (Kennicutt 1998) can be used to convert the $L_{\rm FIR,tot}$ (derived in Section 3.3) into a star formation rate (SFR). Using the conversion, ${\rm SFR}({\rm M}_\odot\ {\rm yr}^{-1}) = 4.5 \times 10^{-44} L_{\rm FIR,tot}({\rm erg\ s}^{-1})$, and the

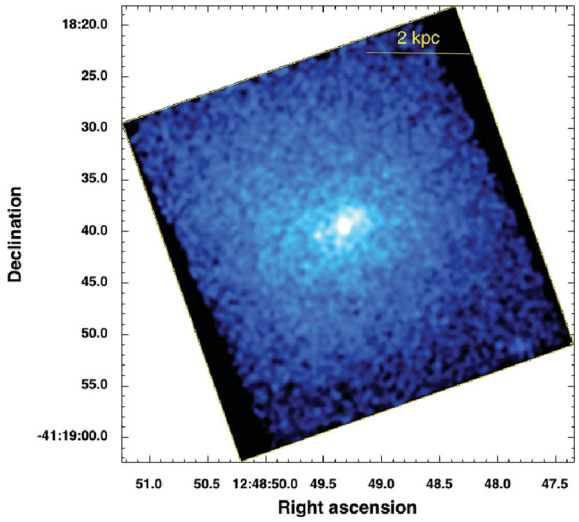

Figure 5. The ACS/SBC FUV *F150LP* observations of NGC 4696 with the *HST* showing a core surrounded by some diffuse low brightness emission. The extent of the FUV emission is very small relative to Hα and [C II]. Weak FUV emission is consistent with the low SFR derived in Section 3.5 and small values of the FUV intensity field, $G0$, described in Section 5.

derived $L_{\rm FIR,tot}$, we obtained a SFR of $\sim$0.13 $M_\odot$ yr^{-1}. However, we expect a non-negligible contribution also from the general stellar radiation field, including the OSP in the host galaxy, which will lower the estimated SFR. Hence, the above value is an upper limit.

We also retrieved far-ultraviolet (FUV) data from the *HST* archive. The data (proposal ID 11681) were taken with the Advanced Camera of Surveys Solar Blind Channel (ACS/SBC) providing a field of view of 34.6 $\times$ 30.5 arcsec^2. These observations were made with two long-pass filters, *F150LP* and *F165LP*, and we chose the *F150LP* filter over *F165LP* to estimate the SFR (described below) due to its higher system throughput.

We used a STARBURST99 stellar library (Leitherer et al. 1999) to model a spectrum of a YSP (whose oldest stars are 10^7 yr old) with a continuous SFR of 0.1 $M_\odot$ yr^{-1}. We fed the output spectrum into the SYNPHOT synthetic photometry package to determine the expected flux in the *F150LP* band. The ratio of the extinction-corrected observed flux to the expected flux from SYNPHOT multiplied by the assumed SFR in STARBURST99 gives a measure of the actual SFR. The FUV emission in the *F150LP* band, shown in Fig. 5, contains a bright core surrounded by low brightness emission. The low surface brightness extended emission is most probably dominated by the passive stellar population. Hence, we derived an upper limit to the SFR based on the assumption that the entire observed FUV emission arises due to a YSP and a lower limit based on the assumption that only the bright core is associated with an ongoing star formation. The measured flux using aperture photometry is 1.23 $\times$ 10^{-15} erg s^{-1} cm^{-2} Å^{-1} if a region of radius $\sim$1.5kpc is considered, which encompasses the bright core as well as the diffuse emission surrounding it, and 2.75 $\times$ 10^{-17} erg s^{-1} cm^{-2} Å^{-1} if only the bright core of radius $\sim$0.5 kpc is considered. These values were corrected for Galactic extinction based on the measured $E(B-V) = 0.113$ from NASA/IPAC Extragalactic Database and the extinction law, $R_V = 3.1[\equiv A(V)/E(B-V)]$ (Cardelli, Clayton & Mathis 1989). The extinction was calculated using the mean R_V-dependent extinction law from Cardelli et al. (1989) in the UV and FUV regime at the pivot wavelength, $\lambda = 1612.236$ Å. The extinction-corrected fluxes are 2.80 $\times$ 10^{-15} and 6.27 $\times$ 10^{-17} erg s^{-1} cm^{-2} Å^{-1}. Note that there is likely to be internal extinction within NGC 4696 and the SFR limits derived below may increase once this additional extinction is taken into account. Comparing the expected flux from the STARBURST99 model to the observed corrected flux gives an upper limit of the FUV-derived SFR of 0.08 $M_\odot$ yr^{-1} and a lower limit of 0.002 $M_\odot$ yr^{-1}. The upper value is in agreement with the upper limit derived from the FIR analysis. This is also consistent with the *GALEX* near-UV (NUV) observations indicative of a SFR consistent with zero and a 3σ upper limit of 0.17 $M_\odot$ yr^{-1}. The *GALEX* analysis takes into account the UV-upturn from an evolved stellar population. The UV excess is calculated by comparing the *GALEX* NUV emission to the Two Micron All Sky Survey (2MASS)[4] K-band emission within an aperture of 35 arcsec and attributed to the ongoing star formation.

The classical X-ray mass deposition rate at a radius of about 35 arcsec from the X-ray peak in the Centaurus galaxy cluster (the projected separation between the X-ray peak and the BCG is 6 arcsec; Mittal et al. 2009) is about (5–9) $M_\odot$ yr^{-1} (e.g. Sanders & Fabian 2008; Hudson et al. 2010). The cooling rates observed in the form of SFR derived from FIR and UV are smaller by about two orders of magnitude. Similarly, Sanders & Fabian (2008) used *XMM–Newton* RGS observations to study the X-ray emission from the core of the Centaurus galaxy cluster. They carried out detailed spectral fitting to measure the amount of gas cooling at the centre and deduced an upper limit of 0.8 $M_\odot$ yr^{-1} below 0.4 keV. This is the standard 'cooling flow' discrepancy, which is resolved when we consider the AGN-regulated feedback. The luminosity of the gas cooling in the centre can be estimated using a cooling flow model in which the gas cools from the virial temperature to a minimum possible lower temperature (0.08 keV). The cooling luminosity is given by

$$L_{\rm cool} = \frac{5}{2}\frac{M_\odot}{\mu m_{\rm p}} kT_{\rm vir}, \quad (4)$$

where $M_\odot$ is the classical mass deposition rate inferred from X-ray observations, $m_{\rm p}$ is the mass of the proton, μ is the mean molecular weight ($\sim$0.65) and $T_{\rm vir}$ is the cluster virial temperature which for Centaurus is about 4 keV. Inserting the estimated $M_\odot$ and $T_{\rm vir}$ gives a cooling luminosity in the range (4.5–8.0) 10^{42} erg s^{-1}. On the heating front, Rafferty et al. (2006) found the mechanical power associated with the AGN-excavated cavities to be 7.4 $\times$ 10^{42} erg s^{-1}. Merloni & Heinz (2007) estimated a similar value for the mechanical power $\sim$7.8 $\times$ 10^{42} erg s^{-1}. Hence there is enough energy in the radio source to balance the cooling of the hot gas and maintain equilibrium.

4 ANALYSIS

4.1 AGN contamination

The interstellar dust is believed to be heated by two principle mechanisms, by young stars and AGN. Hence it may be that some of the IR emission detected is related to the AGN activity. In order to gauge the AGN contribution, diagnostics such as those used by O'Dea et al. (2008) and Quillen et al. (2008), such as the *Spitzer* IRAC 4.5-/3.6-μm colour and [O III] λ5007/Hβ, may be used to discriminate between the presence of an AGN and star formation.

We compiled the optical line emission ratio, [O III] λ5007/Hβ, for NGC 4696 available from Lewis, Eracleous & Sambruna (2003) (<0.4) and Farage et al. (2010) ($\sim$1). The two estimates are not necessarily contradictory since these are calculated over different

[4] http://irsa.ipac.caltech.edu/Missions/2mass.html

apertures. Neither of the ratios indicates a presence of a dominant AGN contribution to the FIR emission. In addition to the low [O III] λ5007/Hβ, the IRAC 4.5-/3.6-μm colour ratio (=0.58) is consistent with a passive stellar population. The absence of the IR [O III] 88-μm spectral feature is another indication of negligible AGN photoionization (Spinoglio 2009).

4.2 Gas kinematics

Observations of NGC 4696 reveal interesting velocity structures, and several studies have used data from different wavebands to study them (e.g. Sparks et al. 1989, 1997; de Jong et al. 1990). The most recent independent investigations by Farage et al. (2010) and Canning et al. (2011b) use observations of Hα at subarcsecond resolution to map the kinematics of the gas.

We used the projected map made using 'specProject' (Section 2.1.2) and obtained a line fit for each individual spaxel separately. The upper panel of Fig. 6 shows the line-of-sight velocity (left) and the line FWHM (right) of the [C II] emission-line gas as inferred with *Herschel*. The *X*- and *Y*-axes are the offsets along RA and Dec. relative to the radio core position corresponding to the 5-GHz very large baseline array (VLBA) core maximum (Taylor et al. 2006). These maps have a nominal scale of 3 arcsec spaxel^{-1}. The lower panel of Fig. 6 shows the line-of-sight velocity (left) and the line FWHM (right) of the Hα+[N II] λ6583 Å emission (Canning et al. 2011b). The Hα+[N II] λ6583 Å integral field unit (IFU) observations were performed with the VIMOS instrument mounted on Melipal, an 8-m telescope at Paranal Observatory.

The line-of-sight velocity of the [C II] emission varies from −115 to 120 km s^{-1}. The gas is blueshifted north of the centre (represented by the radio core), and redshifted south of the centre. This is consistent with the velocity map derived from Hα+[N II] λ6583 Å emission which shows a similar range in the gas velocity and shows that there is gas receding in the south and approaching in the north. These results are also in agreement with the velocity maps presented by Farage et al. (2010) using the Wide Field Spectrograph (WiFeS) instrument that operates on the Australian National University (ANU) 2.3-m telescope at Siding Spring Observatory. Fig. 2 shows that the spatial morphology of the [C II] emission closely follows that of the X-ray and optical spiral filaments. Additionally, the velocity maps show very similar gas kinematics in the IR and the optical. The velocity and emission maps from [C II] and Hα suggest

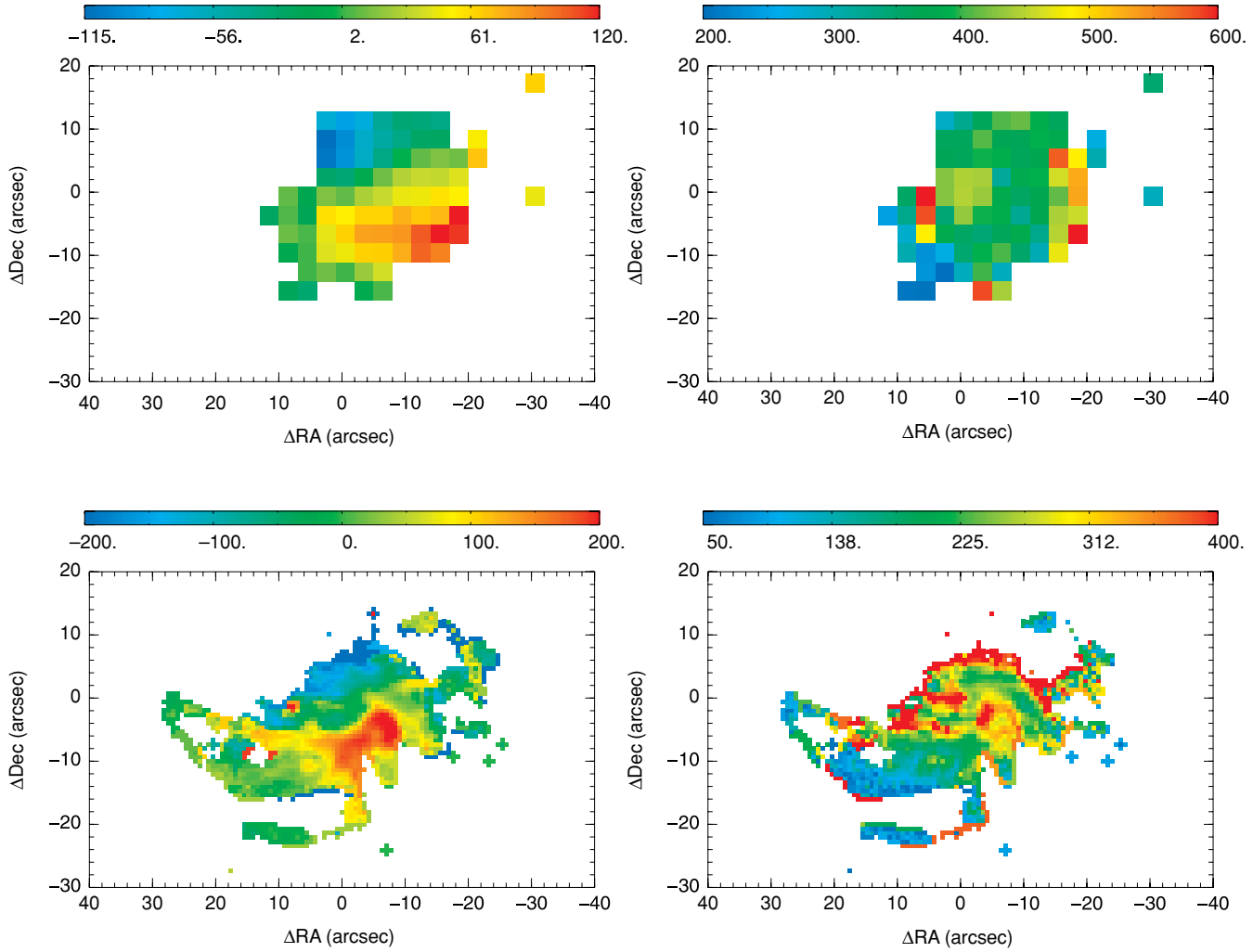

Figure 6. Gas kinematics. The measured line-of-sight velocities (left-hand panels) and line FWHM (right-hand panels) in km s^{-1} of the FIR [C II] gas with a scale 3 arcsec pixel^{-1} (upper panel) and the optical Hα+[N II] λ6583 Å gas with scale 0.67 arcsec pixel^{-1} (lower panel). The velocity dispersion maps have been corrected for the instrumental resolution (235 km s^{-1} for [C II] and 42 km s^{-1} for Hα). The FIR [C II] emission traces the optical Hα emission morphologically and kinematically.

a geometry with gas infalling on a spiral trajectory starting east of the galaxy centre. The trajectory loops around the galaxy in an anticlockwise direction, such that the infalling gas in the south appears to be receding in the rest frame of the galaxy, hence redshifted. The trajectory continues and loops around the galaxy towards the centre, such that the gas in the north appears to be approaching in the rest frame of the galaxy, hence blueshifted.

The velocity dispersion of the [C II] gas ranges from 200 to 600 km s^{-1}. This is slightly larger than the velocity dispersion in the Hα+[N II] λ6583 Å gas from the VLT/VIMOS observations (50–400 km s^{-1}) and also from the WiFeS observations (60–525 km s^{-1}). The larger values for the FIR [C II] data than the optical Hα data are very likely due to beam smearing, since the resolution of the *Herschel* spectral data (11 arcsec) is a lot coarser than that of the optical data (0.67 arcsec pixel^{-1} for the VLT and 0.5 arcsec pixel^{-1} for WiFeS)

The morphological and kinematical correlation between the FIR forbidden line coolant, [C II], and the optical line filaments is a key result of this work. This correlation has a profound implication, namely that the optical hydrogen recombination line, Hα (Fabian et al. 1982; Crawford et al. 2005b; Farage et al. 2010; Canning et al. 2011b), the optical forbidden lines, [N II] λ6583 Å (Dopita et al. 2010; Farage et al. 2010), the soft X-ray filaments (Crawford et al. 2005b) and the FIR [C II] line all have the same energy source.

5 MODELLING THE INTERSTELLAR MEDIUM OF NGC 4696

To understand the complete picture giving rise to emission in NGC 4696 at different wavebands ranging from X-ray to radio, we performed a detailed investigation of the physical parameters of the ISM of the BCG.

The close spatial correspondence between the [C II] maps, along with the NW–SE elongated dust emission, and the optical Hα maps strongly favours a common heating mechanism for the gas. The excitation source that leads to the optical line emission and FIR coolants remains to be investigated. The *Herschel* observations presented in this paper shed light on a key ingredient of this developing picture. The positive detection of the most luminous FIR coolant of the ISM, [C II], along with [O I] and [N II], dictates the presence of PDRs. In this section, we study the source(s) responsible for heating the PDRs.

PDRs form a sharp interface with adjoining H II/H I and H II regions. Photons from nearby young stars (O and B type) with energies >13.6 eV ionize the hydrogen in the molecular gas, giving rise to an H II region. This is followed by a PDR where FUV photons with energies $6 < h\nu < 13.6$ eV are absorbed by dust grains which re-radiate energy in the form of FIR continuum. About 0.1–1 per cent of the incident energy of the FUV photons is converted into photoelectrons with energies $\leq$1 eV which heat the gas via elastic collisions. With CLOUDY, we attempted to model an integrated H II/PDR cloud, where the output emission originating from the cloud also contains contribution from layers beneath the PDR surface.

5.1 Setting up the CLOUDY simulations

A detailed modelling of the various observed continuum and line emission in NGC 4696 was conducted using the spectral synthesis code for modelling the PDRs, CLOUDY (version 08.00, described by Ferland et al. 1998). CLOUDY models the clouds based on conservation of energy through balancing the cooling and heating rates. The simulations are self-consistent and include chemistry, radiative transfer and thermal balance. The basic ingredients of each simulation comprised an OSP and a YSP, wherein the STARBURST99 synthetic library (Leitherer et al. 1999; Vázquez & Leitherer 2005) was used to model the spectra of both the stellar populations. In addition, a background radiation field was included comprising the cosmic background from radio to X-ray (e.g. Ikeuchi & Ostriker 1986; Vedel, Hellsten & Sommer-Larsen 1994), which also included the cosmic microwave background radiation.

Table 4. Observational constraints. The first column is the quantity, the second column is the measured flux and the third column is the ratio of the measured flux to the [C II] 157.74 μm flux.

Quantity	Value (10^{-15} erg s^{-1} cm^{-2})	$F(\lambda)/F_{\rm C\,II}$
[C II][a] 157 μm	174.7 ± 3.1	1
$F_{\rm FIR}^{a,b}$	$(1.105 \pm 0.119) \times 10^4$	$63.3^{+17.3}_{-6.1}$
[O I][a] 63 μm	57.6 ± 7.7	$0.33^{+0.07}_{-0.09}$
[N II][a] 122 μm	24.9 ± 1.7	$0.13^{+0.01}_{-0.01}$
Hα[c]	79.0 ± 0.9	$0.45^{+0.05}_{-0.05}$
[Si I][a]	<4	<0.023
[O III][a]	<3	<0.017
[O IB][a]	<2	<0.011

[a]This work. [Si I], [O III] and [O IB] are non-detections.
[b]Integrated FIR flux in the range (40–500) μm.
[c]Extinction-corrected Hα from Farage et al. (2010).

For the YSP, we used the same spectrum as that used to derive the FUV SFR in Section 3.5, where the oldest stellar age was set to 10^7 yr, and the SFR was considered to be continuous and equal to 0.1 M$_\odot$ yr^{-1}. For the OSP, the oldest stellar age was set to 10 Gyr, and the mass was fixed to 10^{11} M$_\odot$. Among the specified model parameters were the normalizations for the OSP, $\eta_{\rm OSP}$, and the YSP, $G0$, in units of the Habing (1968) field, where 1 Habing is the interstellar radiation field of 1.6×10^{-3} erg s^{-1} cm^{-2} in the energy range 6–13.6 eV. Another parameter was the total hydrogen density (atomic, molecular, ionized and other hydrogen-bearing molecules) in units of cm^{-3}.

This study and several other studies of NGC 4696 provide observational constraints, which may be exploited to constrain the physical properties of the ISM of the galaxy. The data explicitly used to determine the most likely scenario are listed in Table 4. The error bars on [C II]/$L_{\rm FIR}$ were estimated based on the minimum and maximum of the possible values derived from $L_{\rm FIR}$ calculated with the six *Herschel* + MIPS 24-μm data points and $L_{\rm FIR}$ calculated with the averaged data points in case of duplicate measurements (see Section 3.3). The lower error bar on [O I]/[C II] was derived by integrating the flux over all the spaxels with a S/N > 3 for the [C II] line and a S/N >2 for the [O I] line (because of the lower instrument sensitivity at the wavelength of the [O I] line emission and a generally weaker emission relative to [C II]). The upper error bar on [O I]/[C II] was derived by assigning the spaxels with no [O I] detection but a positive [C II] detection a bare minimum flux equal to the sensitivity of the PACS spectrometer in the third order times the chosen S/N, and likewise for the [C II] line. The error bars on [N II]/[C II] and Hα/[C II] reflect the statistical uncertainties in the measurements.

In addition, Kaneda et al. (2005) found the *Spitzer* Infrared Spectrograph (IRS) spectrum of NGC 4696 to show only one significant PAH feature at 12.7 μm with a flux estimate of

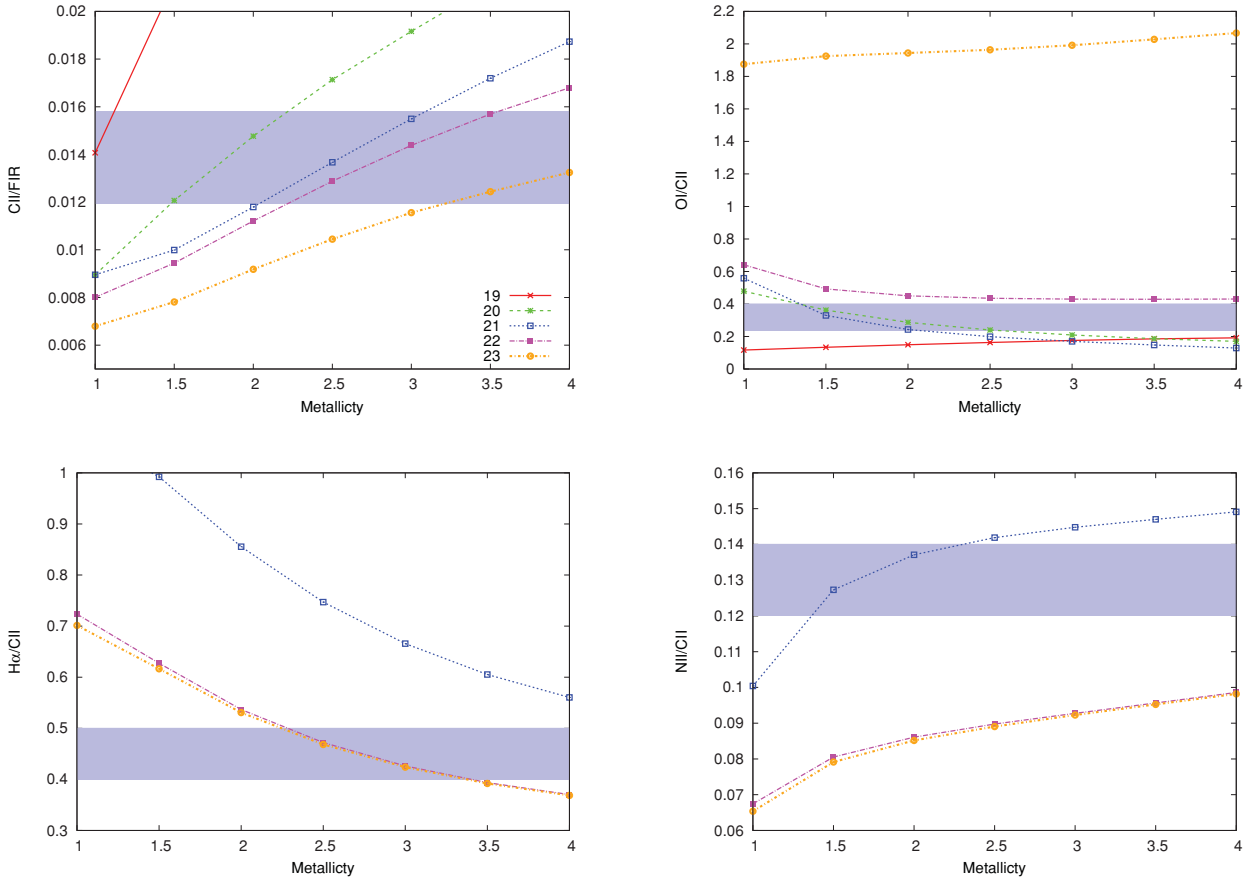

Figure 7. The metallicity and penetration depth dependency of the line ratios, [C II]/$L_{\rm FIR}$ (upper left), [O I]/[C II] (upper right), Hα/[C II] (lower left) and [N II]/[C II] (lower right). The different lines correspond to the different penetration column densities, $N_{\rm H} = 10^{19}$ cm^{-2} (red solid line), 10^{20} cm^{-2} (cyan dashed line), 10^{21} cm^{-2} (dark blue dotted line), 10^{22} cm^{-2} (magenta long-dash–dotted line) and 10^{23} cm^{-2} (orange short-dash–dotted line). The other parameters have been fixed to $G0 = 30$ Habing, $n = 100$ cm^{-3}, $H_{\rm extra} = 10^{-22}$ erg s^{-1} cm^{-3}. The dust and nitrogen abundances are 1.2 and 2 times the default ISM values. The shaded regions correspond to the upper and lower limit of the observed ratios.

14.9×10^{-15} erg s^{-1} cm^{-2}. PAH features are very prominent in the vicinity of young massive stars and so are considered as good tracers of star-forming sites. Absence of any strong PAH features is in concert with the fact that both the FIR- and FUV-derived SFRs are low. Also, even though the dust-to-gas ratio in NGC 4696 is higher than the nominal range (Section 3.4), PAHs owing to their small size are susceptible to grain destruction via physical sputtering or thermal evaporation (Dwek & Arendt 1992; Micelotta, Jones & Tielens 2011). While PAHs have an important effect on the chemistry of PDRs (Bakes & Tielens 1998), due to the lack of any strong PAH features in the IRS spectrum we did not consider PAH grains in our simulations.

The geometry was chosen to be plane parallel by making the inner radius much larger than the thickness of the cloud. The incident radiation from the different stellar populations was input in units of flux (erg s^{-1} cm^{-2}). The simulated output fluxes were determined relative to the [C II] flux and compared to the observations. As a check on the absolute flux levels, we determined the luminosity of the simulated [C II] 157.74-μm line by multiplying the flux with the surface area of the emitting cloud and scaling it to the distance of the Earth. Although the radius of the cloud can be judged from the size of the sphere encompassing the [C II] emission shown in Fig. 6 as $R \sim 17$ arcsec ($\sim$3.5 kpc) (also see Section 3.1), the [C II] flux is not expected to fill up this whole sphere. The volume-filling factor can be determined by equating the simulated and observed fluxes. Note that the PDR model thus constructed is oversimplified in that a single uniform PDR cloud has been assumed. In reality, one expects a distribution of PDR clouds with different and inhomogeneous incident and emergent radiations. However, as shown below, a simple model such as described here is sufficient to study some of the basic physical properties of the ISM in NGC 4696.

X-ray observations of the Centaurus cluster show supersolar abundances in the inner 25 kpc, where the metallicity is $\sim$2 (Graham et al. 2006). Hence we increased the elemental abundances, Z, to two to three times the default ISM values. Furthermore, owing to a small gas-to-dust mass ratio derived in Section 3.4, we increased the dust abundance to 1.2 times the default ISM value leading to a commensurate decrease in the gas-to-dust mass ratio from $\sim$150 to $\sim$70. Another important parameter is the penetration depth of the incident radiation into the PDR cloud. The outer radius of the cloud was specified in terms of the total hydrogen column density, $N_{\rm H}$, at the edge of the cloud (the PDR surface). While the observed ratio of [N II] to [C II] demands relatively low $N_{\rm H}$, the observed ratio of Hα to [C II] demands high $N_{\rm H}$. We investigated a range of $N_{\rm H}$ and Z for the most likely values to explain the observed ratios. The dependency of the ratios on $N_{\rm H}$ and Z is shown in Fig. 7. Based on the results of this investigation, we fixed Z to 2.5 and $N_{\rm H}$ to 10^{21} cm^{-2}. The various model parameters and their input values can be found in Table 5.

Table 5. The basic PDR model parameters. The geometry is assumed to be plane parallel. Columns are as follows: (1) parameter, (2) symbol, (3) the input range and (4) the most likely parameter values.

Parameter	Symbol	Input range	Likely values
Total hydrogen density (cm^{-3})	n	$10–10^6$	50–100
FUV intensity field (Habing[a])	$G0$	$1–10^6$	10–80
Extra heating ($erg\,s^{-1}\,cm^{-3}$)	H_{extra}	10^{-24} to 10^{-20}	$\sim10^{-22}$
Normalization for the OSP[b] ($10^{-16}\,erg\,s^{-1}\,cm^{-2}\,Hz^{-1}$)	η_{OSP}	2.4–156.7	2.4
Hydrogen column density (cm^{-2})	N_H	$10^{19}–10^{23}$	10^{21}
Metallicity	Z	1–4	2.5
Nitrogen abundance (relative to Z)	$Z_\odot$(N)	2–2.5	2

[a]1 Habing $= 1.6 \times 10^{-3}\,erg\,s^{-1}\,cm^{-2}$; [b]old stellar population.

5.2 Photoionization by stars

The aim of conducting these simulations was to understand the key physical ingredients behind the extended [C II] and Hα filaments. Is a YSP important? Can the OSP and YSP alone reproduce the observed ratios listed in Table 4? Do the observational constraints require an additional source of heating? In the AGN-heating regulated feedback framework, the AGN outflows return a fraction of the accreted energy back to the intracluster gas. The radio source can heat the gas either via energetic cosmic ray particles or inflating cavities. The other scenario entailing additional heating revolves around merger-induced shocks in the ISM of the BCG (see Section 6).

The YSP is important in terms of providing FUV photons capable of ionizing carbon to produce the observed [C II] emission. Without any young stars, the [C II]/L_{FIR} ratio cannot be reproduced. This is shown in Fig. 8, where different curves represent different values of η_{OSP}. The OSP produces optical and UV photons which heat up the dust but does not affect the gas much. Hence increasing η_{OSP} has an effect of increasing L_{FIR} but not the intensity of the gas line emissions, which decreases the [C II]/L_{FIR} ratio. Though elementary, this simple exercise underlines the importance of having both the stellar populations. Furthermore, the observed [C II]-to-L_{FIR} ratio ranges from 0.1 per cent in normal and SB galaxies to 1 per cent in dwarf irregular galaxies (Kaufman et al. 1999; Luhman et al. 2003). Edge et al. (2010a,b) studied the [C II]/L_{FIR} ratio in two CC BCGs and found it to be equal to ∼0.4 per cent for Abell 1068 and ∼1.2 per cent for Abell 2597. In comparison, the observed ratio for NGC 4696 is ∼1.6 per cent. Thus the ratio is higher than normal and requires minimum amount of dust heating. While such a large ratio may be reconciled with the PDRs in low-metallicity galaxies with low dust-to-gas mass ratios, NGC 4696 has a very high dust-to-gas mass ratio. In order to reproduce the observed [C II]-to-L_{FIR} ratio, we fixed the η_{OSP} to have a bare minimum value of $2.4 \times 10^{-16}\,erg\,s^{-1}\,cm^{-2}\,Hz^{-1}$. A lower value of η_{OSP} does not produce any discernible effects on the output ratios.

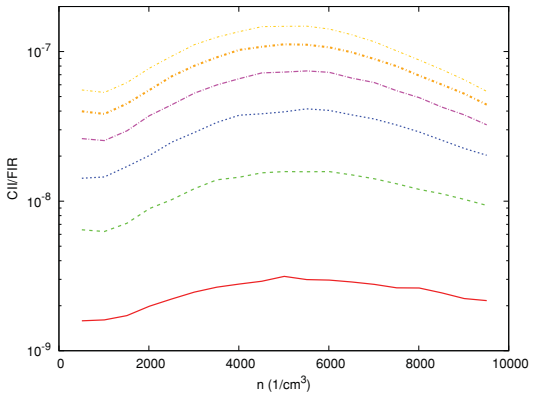

Figure 8. Simulations without any YSP produce low levels of [C II] emission in comparison with the observations. As a result, the [C II]/L_{FIR} ratio is several orders of magnitude below the observed value. The different curves correspond to the different levels of η_{OSP}, the normalization for the OSP, increasing top to bottom from $2.4 \times 10^{-16}\,erg\,s^{-1}\,cm^{-2}\,Hz^{-1}$ (yellow short-dashed dotted line) to $156.7 \times 10^{-16}\,erg\,s^{-1}\,cm^{-2}\,Hz^{-1}$ (red solid line).

Following this, we did simulations based on a model containing both the OSP and YSP, and probed n and $G0$ space ranging from (10 to 10^6) cm^{-3} and (10 to 10^6) Habing. The left-hand panel of Fig. 9 shows the contours of the simulated ratios [O I]/[C II] and [C II]/L_{FIR} corresponding to the lower and upper limit given in Table 4 (where reproducible). We find that the [C II]/L_{FIR} ratio (dotted blue line) saturates at an upper limit of about 0.014, whereas the observed ratio is 0.0147. Also, with this model, the Hα/[C II] ratio is greater than 1 for all values of n and $G0$, whereas the observed ratio is close to 0.45. Since neither the observed [C II]/L_{FIR} nor the Hα/[C II] can be reproduced, we conclude that the model containing only OSP and YSP as the source of heating the PDRs is insufficient to explain the observations of NGC 4696.

5.3 Extra heating

The gas in PDRs is mostly heated via the dust through photoelectric heating. In order to boost the [C II] flux independent of the FIR dust emission, a source of heating is required that may directly input energy to the gas. Thus we included an extra heating term in CLOUDY using the parameter 'hextra', which specifies a volume-heating rate ($erg\,s^{-1}\,cm^{-3}$). The source of this extra heating is unspecified and so may be attributed to either shock heating or cosmic ray heating due to the radio source. We investigated models containing the OSP and YSP and additional heating ranging from 10^{-24} to $10^{-20}\,erg\,s^{-1}\,cm^{-3}$. The term 'hextra' acts to raise the temperature of both the gas and the dust independent of each other. The standard behaviour of [C II] is such that for a given $G0$, the [C II] intensity increases linearly up to the critical density ($n \sim 3000\,cm^{-3}$ for the [C II] forbidden line), beyond which collisional de-excitation occurs as often as radiation. Hence the line intensity above the critical density is not very sensitive to the density and increases with it only very slowly. The extra heating acts to boost the [C II] intensity at low densities all the way up to $n \sim 10^4\,cm^{-3}$, after which it decreases due to overly suppressed radiative de-excitation. The extra heating also increases the dust emission; however, the increase is roughly independent of the density. The overall effect of the heating term on the [C II]/L_{FIR} ratio is such that the ratio increases for low densities, where the increase in [C II] is larger than the increase in L_{FIR}.

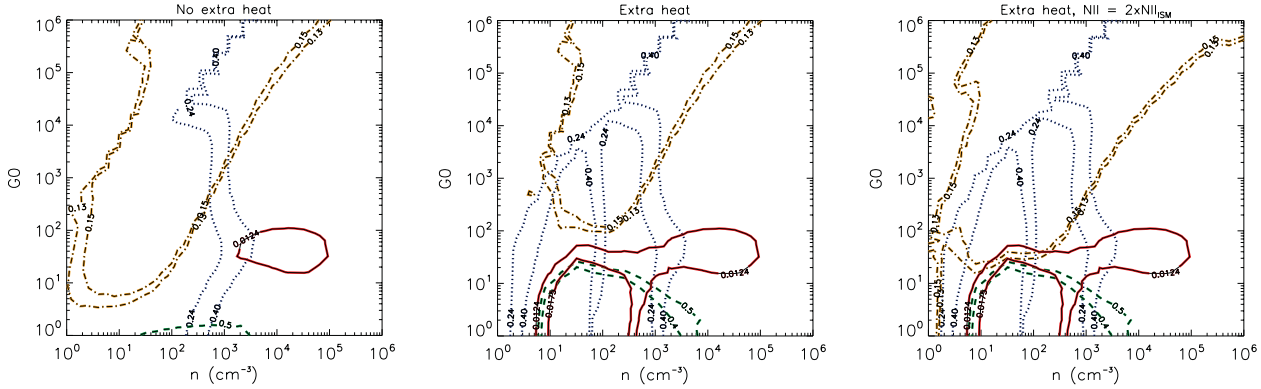

Figure 9. Simulations containing both OSP and YSP. The dust abundance is set to 1.2 times the ISM value, and the metallicity is set to 2.5 times the ISM value. Shown are the contours corresponding to the lower and upper observed limits (where reproducible) for [C II]/$L_{\rm FIR}$ (solid red line), [O I]/[C II] (dotted blue line), Hα/[C II] (dashed green line) and [N II]/[C II], (dot–dashed mustard line). Left: heating by stars only. Middle: heating by stars and an additional source, such as cosmic rays, shocks, etc. Right: nitrogen overabundance of a factor of 2.

The middle panel of Fig. 9 shows the contours of [C II]/$L_{\rm FIR}$ (solid red), [O I]/[C II] (dotted blue) and Hα/[C II] (dashed green) for $H_{\rm extra} = 10^{-22}$ erg s^{-1} cm^{-3}. Of the different levels of $H_{\rm extra}$ investigated, this was the optimal value leading to most coherent results. For example, $H_{\rm extra} = 10^{-21}$ erg s^{-1} cm^{-3} fails to reproduce the observed [O I]/[C II] ratio, and $H_{\rm extra} = 10^{-23}$ erg s^{-1} cm^{-3} just barely touches the observed [C II]/$L_{\rm FIR}$ ratio. We found that while $H_{\rm extra}$ could reproduce the right levels of [C II]/$L_{\rm FIR}$, Hα/[C II] and [O I]/[C II], the [N II]/[C II] ratio was too low compared to the observations. The FIR [N II] line emission (the first ionization potential of nitrogen is 14.5 eV) arises from warm ionized medium only, whereas [C II] emission can arise from both neutral (PDRs) and ionized media. The fraction of [C II] emission arising from ionized media is highly uncertain, ranging from 25 per cent up to more than 50 per cent (e.g. Heiles 1994; Aannestad & Emery 2003; Oberst et al. 2006). However, since our model includes a PDR adjacent to an H II region, the total [C II] emission includes contributions from both, neutral as well as ionized media, and no correction factor is needed to estimate the fraction of [C II] emission arising from the PDR alone. The right-hand panel of Fig. 9 corresponds to the same setting as for the middle panel, only the nitrogen abundance, $Z_{\odot}$(N), has been increased by a factor of 2 over the ISM value. The contours corresponding to the [N II]/[C II] ratio (dot–dashed mustard) now overlap with the contours of the [C II]/$L_{\rm FIR}$, [O I]/[C II] and Hα/[C II] ratios. A nitrogen overabundance from the PDR analysis is consistent with the enhancement in nitrogen abundance required based on the optical line ratios (Farage et al. 2010) and X-ray spectral fitting (Sanders et al. 2008). The fact that the analyses of the NGC 4696 observations in X-ray, optical and FIR wavebands all require a nitrogen overabundance and by roughly the same factor is reassuring and lends support to the above PDR model.

The emanating [C II] flux from the cloud is about 1×10^{-3} erg s^{-1} cm^{2}. The size of the cloud that results in the observed [C II] flux is such that $F_{\rm C\,II,obs} = F_{\rm C\,II,mod} \times (r/D_{\rm L})^2$, where $F_{\rm C\,II,obs}$ is the observed [C II] line flux and $F_{\rm C\,II,mod}$ is the modelled [C II] line flux, r is the 'effective radius' of the cloud and $D_{\rm L}$ is the luminosity distance to NGC 4696. The radius of the cloud thus calculated is $r = 0.5$ kpc. Considering that the [C II] flux extends over a $\sim$3.5 kpc large region implies a volume filling factor of $\sim 3 \times 10^{-3}$.

These PDR simulations help us to narrow down the most probable heating scenario such that it simultaneously reproduces all the observed line and continuum ratios. The most likely parameter values are given in the last column of Table 5. The right-hand panel of Fig. 9 is based on a model that contains photoionization from OSP and YSP, and an additional source of heating. Note that photoionization from young stars is still of paramount importance. A model containing only extra heating and no young stars produces very little [C II] because of severe lack on FUV photons. The model containing stars and 'extra heating' best explains the observations yielding a density, n, in the range of about a few tens to hundred per cm^3 and a radiation field, $G0$, in the range from 10 to $\sim$80 Habing. This range of $G0$ corresponds to a SFR of (0.02–0.13) M$_{\odot}$ yr^{-1} for a cloud of an effective radius of 0.5 kpc. The SFR thus estimated agrees very well with the limits derived from the FIR and NUV/FUV observations (Section 3.5).

6 DISCUSSION

The Centaurus cluster of galaxies can be classified as a strong CC cluster based on its short gas cooling time (<0.5 Gyr) and a peaked X-ray surface brightness profile. The mass condensation rate derived from the FIR and UV observations is small ($\sim$0.1 M$_{\odot}$ yr^{-1}) as compared to that predicted based on the cooling flow model ($\sim$25 M$_{\odot}$ yr^{-1}). The X-ray core luminosity at 2.5 per cent R_{500} corresponding to a region of radius 30 kpc is about 1.3×10^{43} erg s^{-1} (Sanders et al. 2008). This is the amount of power (radiative losses) that needs to be fed back to the ICM over that scale for the system to remain in equilibrium. One of the potential feedback mechanisms is through the expanding radio plasma that has dug out multiple cavities in the ICM of NGC 4696 at radii $\leq$6 kpc. The power in these radio bubbles assuming a buoyancy time-scale is estimated to be about 0.7×10^{43} erg s^{-1} (Rafferty et al. 2006). Repetitive inflation of such radio bubbles also creates sound waves which generate a sound wave power of about 0.5×10^{43} erg s^{-1} (Sanders et al. 2008). These two mechanisms together suffice to balance the X-ray radiative losses and can keep the central region of Abell 3526 in quasi-equilibrium.

The optical and FIR line emissions clearly show an infalling gas flow of spiral pattern. There are two possibilities for the origin of the gas and dust. The first possibility is that this material represents the cooling ICM flowing towards the centre of the dark matter potential well (which in the case of Centaurus coincides with the BCG). The fact that the soft X-ray emission (0.5–1) keV traces the spiral structure seen in Hα and [C II] does indeed suggest a link to the gas cooling out of the ICM. The relative increase in the X-ray surface brightness along the filaments is a natural outcome of this scenario.

Fabian et al. (2011) examined the *Chandra* X-ray emission from the northern filament in the Perseus cluster and provided another outlook on the excitation mechanism of the filaments. Their results indicate that some of the soft X-ray emission may be due to charge exchange as the hot ionized gas penetrates and mixes with cold gas. Although the cooling flow model does not dictate a coherent directional gas flow to the centre, such as that seen in NGC 4696, the spiral morphology may be a natural consequence of the global velocity field of the gas surrounding NGC 4696. This may be the first direct mapping of a cooling flow in a galaxy cluster.

The second possibility is that the filaments and the dust lane in NGC 4696 have a galaxy infall origin. This is based on a merger hypothesis proposed by Sparks et al. (1989) and more recently by Farage et al. (2010). Under this hypothesis, the BCG is undergoing a minor merger with an infalling neighbouring dust-rich galaxy. The presence of two nuclei in *HST* imaging of the centre of NGC 4696 (Laine et al. 2003) lends some support to the merger hypothesis, although the nature of the second nucleus is not well established. A merger hypothesis also explains the prominent dust lane seen with the *HST*. While Sparks et al. (1989) favour heat transfer via conduction from the hot X-ray-emitting ICM to the cool dust-rich infalling gas, Farage et al. (2010) favour shock heating generated through the dissipation of the orbital energy of the infalling cloud. Assuming a shock luminosity of 2×10^{42} erg s^{-1} (Farage et al. 2010), the shock volume luminosity over a region of radius 0.5 kpc is 1.3×10^{-22} erg s^{-1} cm^{-3}. This is in good agreement with the level of the extra heating input to the simulations above.

Irrespective of the origin of the cold gas and dust, the detailed PDR modelling of the observed quantities arising from this flow (described in Section 5) shows photoionization from stars is an important requisite. However, there is an additional source of energy input required to reproduce the observables. This additional source of heating could represent either the energy deposited by the AGN through the methods described above or shock heating due to a minor merger. The additional heating amounts to <10 per cent of the X-ray core luminosity and could be another contributing factor to the total heating budget.

The non-radiative energy sources, in principle, could be input into the simulations either in the form of extra heating (shock heating or reconnection diffusion; see Fabian et al. 2011, for the latter), such as that considered in these CLOUDY simulations, or cosmic rays. Ferland et al. (2008, 2009) have shown that while it is difficult to differentiate between the two processes, certain optical lines could help discriminate between the two. The extra heating case in those studies has primarily been associated with magnetohydrodynamic (MHD) waves such as those observed in the ISM of our galaxy. The dissipation of MHD wave energy can heat the gas; however, the heating simply adds to the thermal energy of the gas so that the velocity distribution remains Maxwellian. On the other hand, the cosmic ray heating by high-energy particles can both heat and ionize the gas. Both the processes heat the gas, but the cosmic ray (ionizing particle) case produces a population of first and second ions by non-thermal collisional ionization. In the extra heating case, these ions only occur when the gas is warm enough for collisional ionization equilibrium to occur. This is the main distinction between the two cases, extra heating and cosmic ray heating.

Ferland et al. (2009) studied the Horseshoe region of the Perseus galaxy cluster and used the IR and optical line intensities to distinguish between extra heating and cosmic ray heating. They found that both the heating cases match the observations to within a factor of 2 for the majority of the lines. There are a few discriminant lines, such as the optical emissions [He I] λ5876 Å and [Ne III] λ3869 Å and the IR emission [Ne II] λ12.81 μm which show a few orders of magnitude difference and indicate that the cosmic ray may be a better agent for heating and ionizing the gas (also see Donahue et al. 2011). The mid-IR *Spitzer* IRS spectrum of the off-centre regions of NGC 4696, in fact, contains the [Ne II] λ12.81 μm line (Johnstone et al. 2007). This along with the detections of rovibrational H_2 lines in off-nuclear regions in NGC 4696 and NGC 1275 provided some of the motivation for the heating models investigated by Ferland et al. (2009). However, previous studies did not consider the lines observed with *Herschel*, which provide a crucially important perspective on the physical model of the ISM.

Though our model contains additional energy explicitly in the form of extra heating, we speculate the ionizing particle model would also have fitted the available data, as has been shown for Perseus. In order to discern the two heating sources, deep optical observations are needed to complement the *Herschel* data.

7 SUMMARY

We made FIR observations of the brightest galaxy, NGC 4696, of the Centaurus galaxy cluster with the *Herschel* telescope to better understand the cooling and heating of the ICM.

(i) We have detected FIR coolants in NGC 4696, which include extended [C II] 157.74 μm, marginally extended [O I] 63.18 μm and unresolved [N II] 121.90 μm line emissions.

(ii) We have detected FIR dust emission from the BCG at 70, 100, 160, 250, 350 and 500 μm. An SED fitting of the dust emission reveals a high-mass cold component around 19 K and a low-mass warm component around 60 K.

(iii) Using the dust mass calculated from the SED fitting and the non-detection of CO (O'Dea et al. 1994), we derived an upper limit on the gas-to-dust mass ratio of 125. This makes NGC 4696 a galaxy with one of the lowest gas-to-dust mass ratios.

(iv) The SFR derived from the integrated FIR luminosity is about 0.13 $M_\odot$ yr^{-1}. We derived similar upper limits from *HST* FUV and *GALEX* near-UV observations.

(v) The extended [C II]-emitting gas shows remarkably similar spatial morphology and kinematics as the optical Hα-emitting and X-ray gas. This implies a common heating mechanism of the gas.

(vi) We envisage the FIR and optical emissions as arising from PDRs adjacent to ionized regions. From a detailed modelling of such an integrated PDR, we conclude that in addition to heating via stellar photoionization, an additional non-radiative heating is required. The most likely model yields a total hydrogen density in the range (50–100) cm^{-3} and a FUV intensity field in the range (10–80) Habing.

ACKNOWLEDGMENTS

This work is based (in part) on observations made with *Herschel*, a European Space Agency Cornerstone Mission with significant participation by NASA. Support for this work was provided by NASA through an award issued by JPL/Caltech. We would like to thank the HSC and NHSC consortium for support with data-reduction pipelines. RM is grateful to P. Appleton for repeated help with the *Herschel* analysis and thanks J. T. Whelan and D. Merritt for comments and discussions. BRMcN and HR acknowledge generous financial support from the Canadian Space Agency Space Science Enhancement Programme. NAH thanks STFC and the University of Nottingham Anne McLaren Fellowship for support. GT acknowledges support from the New York Space Grant Consortium. This

research has made use of the NASA/IPAC Extragalactic Database (NED) which is operated by the JPL/Caltech, under contract with NASA. STSDAS is a product of the Space Telescope Science Institute, which is operated by AURA for NASA.

REFERENCES

Aannestad P. A., Emery R. J., 2003, A&A, 406, 155
Allen S. W., 1995, MNRAS, 276, 947
Allen S. W., Fabian A. C., 1994, MNRAS, 269, 409
Aravena M. et al., 2008, A&A, 491, 173
Bakes E. L. O., Tielens A. G. G. M., 1998, ApJ, 499, 258
Binney J., Tabor G., 1995, MNRAS, 276, 663
Bîrzan L., Rafferty D. A., McNamara B. R., Wise M. W., Nulsen P. E. J., 2004, ApJ, 607, 800
Bregman J. N., Fabian A. C., Miller E. D., Irwin J. A., 2006, ApJ, 642, 746
Burns J. O., 1990, AJ, 99, 14
Canning R. E. A., Fabian A. C., Johnstone R. M., Sanders J. S., Crawford C. S., Hatch N. A., Ferland G. J., 2011a, MNRAS, 411, 411
Canning R. E. A. et al., 2011b, MNRAS, submitted
Cardelli J. A., Clayton G. C., Mathis J. S., 1989, ApJ, 345, 245
Churazov E., Sunyaev R., Forman W., Böhringer H., 2002, MNRAS, 332, 729
Conselice C. J., Gallagher J. S., III, Wyse R. F. G., 2001, AJ, 122, 2281
Crawford C. S., Allen S. W., Ebeling H., Edge A. C., Fabian A. C., 1999, MNRAS, 306, 857
Crawford C. S., Sanders J. S., Fabian A. C., 2005a, MNRAS, 361, 17
Crawford C. S., Hatch N. A., Fabian A. C., Sanders J. S., 2005b, MNRAS, 363, 216
de Jong T., Norgaard-Nielsen H. U., Jorgensen H. E., Hansen L., 1990, A&A, 232, 317
Donahue M., Mack J., Voit G. M., Sparks W., Elston R., Maloney P. R., 2000, ApJ, 545, 670
Donahue M., de Messières G. E., O'Connell R. W., Voit G. M., Hoffer A., McNamara B. R., Nulsen P. E. J., 2011, ApJ, 732, 40
Dopita M. et al., 2010, Ap&SS, 327, 245
Dunn R. J. H., Fabian A. C., 2006, MNRAS, 373, 959
Dunne L., Eales S. A., 2001, MNRAS, 327, 697
Dunne L., Eales S., Edmunds M., Ivison R., Alexander P., Clements D. L., 2000, MNRAS, 315, 115
Dwek E., Arendt R. G., 1992, ARA&A, 30, 11
Edge A. C., 2001, MNRAS, 328, 762
Edge A. C., Frayer D. T., 2003, ApJ, 594, L13
Edge A. C., Wilman R. J., Johnstone R. M., Crawford C. S., Fabian A. C., Allen S. W., 2002, MNRAS, 337, 49
Edge A. C. et al., 2010a, A&A, 518, L46
Edge A. C. et al., 2010b, A&A, 518, L47
Edwards L. O. V., Hudson M. J., Balogh M. L., Smith R. J., 2007, MNRAS, 379, 100
Fabian A. C., 1994, ARA&A, 32, 277
Fabian A. C., Nulsen P. E. J., Atherton P. D., Taylor K., 1982, MNRAS, 201, 17p
Fabian A. C., Celotti A., Blundell K. M., Kassim N. E., Perley R. A., 2002, MNRAS, 331, 369
Fabian A. C., Sanders J. S., Taylor G. B., Allen S. W., 2005, MNRAS, 360, L20
Fabian A. C., Sanders J. S., Williams R. J. R., Lazarian A., Ferland G. J., Johnstone R. M., 2011, MNRAS, 417, 172
Farage C. L., McGregor P. J., Dopita M. A., Bicknell G. V., 2010, ApJ, 724, 267
Ferland G. J., Korista K. T., Verner D. A., Ferguson J. W., Kingdon J. B., Verner E. M., 1998, PASP, 110, 761
Ferland G. J., Fabian A. C., Hatch N. A., Johnstone R. M., Porter R. L., van Hoof P. A. M., Williams R. J. R., 2008, MNRAS, 386, L72
Ferland G. J., Fabian A. C., Hatch N. A., Johnstone R. M., Porter R. L., van Hoof P. A. M., Williams R. J. R., 2009, MNRAS, 392, 1475
Graham J., Fabian A. C., Sanders J. S., Morris R. G., 2006, MNRAS, 368, 1369
Griffin M. J. et al., 2010, A&A, 518, L3
Habing H. J., 1968, Bull. Astron. Inst. Netherlands, 19, 421
Hatch N. A., Crawford C. S., Fabian A. C., Johnstone R. M., 2005, MNRAS, 358, 765
Heckman T. M., Baum S. A., van Breugel W. J. M., McCarthy P., 1989, ApJ, 338, 48
Heiles C., 1994, ApJ, 436, 720
Hicks A. K., Mushotzky R., 2005, ApJ, 635, L9
Hollenbach D. J., Tielens A. G. G. M., 1999, Rev. Modern Phys., 71, 173
Hollenbach D. J., Takahashi T., Tielens A. G. G. M., 1991, ApJ, 377, 192
Hu E. M., Cowie L. L., Wang Z., 1985, ApJS, 59, 447
Hudson D. S., Mittal R., Reiprich T. H., Nulsen P. E. J., Andernach H., Sarazin C. L., 2010, A&A, 513, A37
Ikebe Y., Makishima K., Fukazawa Y., Tamura T., Xu H., Ohashi T., Matsushita K., 1999, ApJ, 525, 58
Ikeuchi S., Ostriker J. P., 1986, ApJ, 301, 522
Jaffe W., Bremer M. N., 1997, MNRAS, 284, L1
Johnstone R. M., Fabian A. C., Nulsen P. E. J., 1987, MNRAS, 224, 75
Johnstone R. M., Hatch N. A., Ferland G. J., Fabian A. C., Crawford C. S., Wilman R. J., 2007, MNRAS, 382, 1246
Kaastra J. S., Ferrigno C., Tamura T., Paerels F. B. S., Peterson J. R., Mittaz J. P. D., 2001, A&A, 365, L99
Kaneda H., Onaka T., Sakon I., 2005, ApJ, 632, L83
Kaneda H., Onaka T., Kitayama T., Okada Y., Sakon I., 2007, PASJ, 59, 107
Kaufman M. J., Wolfire M. G., Hollenbach D. J., Luhman M. L., 1999, ApJ, 527, 795
Kennicutt R. C., Jr, 1998, ARA&A, 36, 189
Laine S., van der Marel R. P., Lauer T. R., Postman M., O'Dea C. P., Owen F. N., 2003, AJ, 125, 478
Leitherer C. et al., 1999, ApJS, 123, 3
Levenberg K., 1944, Q. Applied Math., 2, 164
Lewis K. T., Eracleous M., Sambruna R. M., 2003, ApJ, 593, 115
Lucey J. R., Currie M. J., Dickens R. J., 1986, MNRAS, 221, 453
Luhman M. L., Satyapal S., Fischer J., Wolfire M. G., Sturm E., Dudley C. C., Lutz D., Genzel R., 2003, ApJ, 594, 758
McNamara B. R., Nulsen P. E. J., 2007, ARA&A, 45, 117
McNamara B. R., O'Connell R. W., 1989, AJ, 98, 2018
Marquardt D., 1963, SIAM J. Applied Math., 11, 431
Merloni A., Heinz S., 2007, MNRAS, 381, 589
Micelotta E. R., Jones A. P., Tielens A. G. G. M., 2011, A&A, 526, A52
Mittal R., Hudson D. S., Reiprich T. H., Clarke T., 2009, A&A, 501, 835
Mittaz J. P. D. et al., 2001, A&A, 365, L93
Oberst T. E. et al., 2006, ApJ, 652, L125
O'Dea C. P., Baum S. A., Maloney P. R., Tacconi L. J., Sparks W. B., 1994, ApJ, 422, 467
O'Dea C. P., Baum S. A., Mack J., Koekemoer A. M., Laor A., 2004, ApJ, 612, 131
O'Dea C. P. et al., 2008, ApJ, 681, 1035
O'Dea K. P. et al., 2010, ApJ, 719, 1619
Oegerle W. R., Cowie L., Davidsen A., Hu E., Hutchings J., Murphy E., Sembach K., Woodgate B., 2001, ApJ, 560, 187
Ott S., 2010, in Mizumoto Y., Morita K. I., Ohishi M., eds, ASP Conf. Ser. Vol. 434, Astronomical Data Analysis Software and Systems XIX. Astron. Soc. Pac., San Francisco, p. 139
Peterson J. R., Fabian A. C., 2006, Phys. Rep., 427, 1
Peterson J. R. et al., 2001, A&A, 365, L104
Peterson J. R., Kahn S. M., Paerels F. B. S., Kaastra J. S., Tamura T., Bleeker J. A. M., Ferrigno C., Jernigan J. G., 2003, ApJ, 590, 207
Pilbratt G. L. et al., 2010, A&A, 518, L1
Poglitsch A. et al., 2010, A&A, 518, L2
Postman M., Lauer T. R., 1995, ApJ, 440, 28
Quillen A. C. et al., 2008, ApJS, 176, 39
Rafferty D. A., McNamara B. R., Nulsen P. E. J., Wise M. W., 2006, ApJ, 652, 216
Röllig M. et al., 2007, A&A, 467, 187
Roychowdhury S., Ruszkowski M., Nath B. B., Begelman M. C., 2004, ApJ, 615, 681

Sakelliou I. et al., 2002, A&A, 391, 903
Salomé P., Combes F., 2003, A&A, 412, 657
Salomé P., Combes F., Revaz Y., Edge A. C., Hatch N. A., Fabian A. C., Johnstone R. M., 2008, A&A, 484, 317
Sanders J. S., Fabian A. C., 2002, MNRAS, 331, 273
Sanders J. S., Fabian A. C., 2008, MNRAS, 390, L93
Sanders J. S., Fabian A. C., Allen S. W., Morris R. G., Graham J., Johnstone R. M., 2008, MNRAS, 385, 1186
Sparks W. B., Macchetto F., Golombek D., 1989, ApJ, 345, 153
Sparks W. B., Carollo C. M., Macchetto F., 1997, ApJ, 486, 253
Spinoglio L., 2009, in Pagani L., Gerin M., eds, EAS Publ. Ser. Vol. 34, Astronomy in the Submillimeter and Far Infrared Domains with the Herschel Space Observatory. EDP Sciences, Les Ulis, p. 237
Tamura T. et al., 2001, A&A, 365, L87
Taylor G. B., Sanders J. S., Fabian A. C., Allen S. W., 2006, MNRAS, 365, 705
Vázquez G. A., Leitherer C., 2005, ApJ, 621, 695
Vedel H., Hellsten U., Sommer-Larsen J., 1994, MNRAS, 271, 743
Voit G. M., Donahue M., 2005, ApJ, 634, 955
Wolfire M. G., Tielens A. G. G. M., Hollenbach D., 1990, ApJ, 358, 116
Xu H. et al., 2002, ApJ, 579, 600

This paper has been typeset from a TEX/LATEX file prepared by the author.